

STATIC BUCKLING AND POSTBUCKLING CHARACTERISTICS OF THIN-WALL ALUMINUM CYLINDERS UNDER ECCENTRIC COMPRESSIVE AXIAL LOADS

James J. Kotanchik

Emmett A. Witmer

Theodore H. H. Pian

December 1964

Prepared for

BALLISTIC SYSTEMS DIVISION

AIR FORCE SYSTEMS COMMAND

NORTON AIR FORCE BASE, CALIFORNIA

Aeroelastic and Structures Research Laboratory

Department of Aeronautics and Astronautics

Massachusetts Institute of Technology

Cambridge, Massachusetts 02139

Best Available Copy

ABSTRACT

Results from experimental measurements of buckling threshold and postbuckling characteristics of thin-wall aluminum-alloy circular cylinders loaded at various fixed ratios of axial compressive load to applied bending moment are reported. Buckling modes, both symmetric and antisymmetric, with respect to the plane of loading occurred and are presented. Typical results are shown. Postbuckling measurements of load-deflection characteristics are extended to very large deflections, and include a number of measurements during unloading and reversed loading.

TABLE OF CONTENTS

<u>Section</u>		<u>Page</u>
I	INTRODUCTION	1
II	DESCRIPTION OF CYLINDRICAL TEST SPECIMENS AND STRESS-STRAIN MEASUREMENTS	4
	2.1 Cylindrical Test Specimens	4
	2.2 Material Stress-Strain Measure- ments and Results	4
III	TESTS AND PROCEDURE	6
	3.1 Cylinders in Pure Bending	6
	3.2 Cylinders under Combined Axial and Bending Loads	7
IV	TEST RESULTS AND DISCUSSION	9
	4.1 Buckling-Mode Features	9
	4.2 Incipient-Buckling Results	10
	4.3 Postbuckling Load-Deflection Characteristics	10
REFERENCES		18
TABLES		20
FIGURES		21

LIST OF ILLUSTRATIONS

<u>Figure</u>		<u>Page</u>
1	Material Stress-Strain Measurements	21
2	Illustration of Typical Shell Wall Thickness Distribution for a Specimen with $R/t = 100$	22
3	Loading Schematics and Nomenclature	23
4	Loading Arrangement for Pure Moment Tests	24
5	Combined-Loading Test Arrangement Before Buckling of a Test Specimen	25
6	Combined-Loading Test Arrangement After Buckling of a Test Specimen	26
7	Buckled Cylindrical Shells from Pure Bending Tests (Series I and II)	27
8	Buckled Cylindrical Shells from Combined-Loading Tests, $R/t = 50$	28
9	Buckled Cylindrical Shells from Combined-Loading Tests, $R/t = 75$	29
10	Buckled Cylindrical Shells from Combined-Loading Tests, $R/t = 100$	30
11	Illustration and Nomenclature for Symmetric and Antisymmetric Buckle Pattern	31
12	Overall Section View of Shell Buckled in the Symmetric Mode, Specimen V-3	32
13	Sectioned View of a Symmetric Buckle, Specimen V-3	33
14	Section View of a Shell Buckled in the Antisymmetric Mode, Specimen V-4	34

<u>Figure</u>		<u>Page</u>
15	Incipient-Buckling Stress as a Function of R/t and Loading Eccentricity	35
16	Combined-Load Incipient-Buckling Data for Unstiffened Cylinders with R/t Values Ranging from 230 to 800 and L/D Values Ranging from 0.5 to 1.5 [Ref. 2]	36
17	Combined-Load Buckling-Threshold Data for R/t = 50	37
18	Combined-Load Buckling-Threshold Data for R/t = 75	38
19	Combined-Load Buckling-Threshold Data for R/t = 100	39
20	Geometry and Nomenclature for a Buckled Specimen	40
21	Nomenclature and Typical Load-Deflection Characteristics of a Loaded Specimen in Both the Prebuckling and the Postbuckling Regime	41
22	Typical Prebuckling and Postbuckling Moment-Rotation Data for a Specimen Subjected to Pure Bending, R/t = 50	42
23	Typical Prebuckling and Postbuckling Moment-Rotation Data for a Specimen Subjected to Pure Bending, R/t = 75	43
24	Typical Prebuckling and Postbuckling Moment-Rotation and Load-Shortening Data, R/t = 50 and e = 0.016	44
25	Typical Prebuckling and Postbuckling Moment-Rotation and Load-Shortening Data, R/t = 50 and e = 0.25	46
26	Typical Prebuckling and Postbuckling Moment-Rotation and Load-Shortening Data, R/t = 75 and e = 0.016	48

<u>Figure</u>		<u>Page</u>
27	Typical Prebuckling and Postbuckling Moment-Rotation and Load-Shortening Data, $R/t = 75$ and $e = 0.25$	50
28	Typical Prebuckling and Postbuckling Moment-Rotation and Load-Shortening Data, $R/t = 100$ and $e = 0.25$	52

LIST OF TABLES

<u>Table</u>		<u>Page</u>
i	Summary of Test Data	20

SECTION I

INTRODUCTION

Under sufficiently intense blast loading, slender shell structures can undergo buckling and large postbuckling deformations. Depending upon the structural parameters involved, as well as the (asymmetric) distribution and time history of the blast loading, a "bending-type" buckling pattern may occur at one or more axial stations of the structure with the region of severe buckling remaining essentially at a fixed axial station(s) as the postbuckling deformation increases. For other structural parameter and loading conditions, peripheral buckling modes may occur. In the present study, attention is confined to the former type of failure and postfailure behavior.

One of the items of information necessary to permit predicting the postbuckling dynamic and "postblast" final deformation of such structures is the postbuckling load-carrying ability of the structure at the "buckled station" expressed in terms of moment-carrying ability as a function of some characteristic deformation parameter(s). Also, of course, knowledge of the transient blast forces and proper inclusion of the elastic-plastic and inertial forces present are also essential for such predictions. The present report, however, is concerned mainly with the matter of static buckling and postbuckling characteristics for simple shell structures; implicit in this is the intention of employing this static postfailure information as a first approximation in a dynamic structural-response analysis.

Much experimental data have been obtained to define static incipient elastic and/or plastic buckling of unstiffened cylinders as well as for cylinders which are stiffened axially and/or circumferentially [1-6, for example]. However, very little

experimental data exist on the postbuckling load-deformation characteristics of such cylindrical shells [7, 8]; on the other hand, rather detailed experimental postfailure structural characteristics data for complex built-up lifting-surface structures have been obtained [9-13]. The present experiments, therefore, were considered to be necessary to contribute to remedying this information deficiency for cylindrical shells.*

Of the numerous conceivable combinations of loading to which typical slender shells might be subjected, it is believed that combined axial loading and bending of the structure is a typical combination and represents one of perhaps greatest practical interest. Furthermore, simple unstiffened cylindrical shells were chosen for testing as being both typical and free from the additional and, for present purposes, unnecessary complicating factors that the presence of discrete or core stiffeners would entail.

Specifically, the present experimental studies were designed and conducted to provide the following information on simple thin-wall cylindrical shells with R/t values ranging from about 50 to 100:

- (1) Incipient buckling loads* for specimens subjected to
 - (a) pure bending moment, and
 - (b) combined bending and axial compressive loads.
- (2) Postbuckling load-deflection characteristics of cylindrical shells including those under unloading and reversed loading.

* Published incipient buckling data for unstiffened cylinders under these conditions do not include the present R/t range of interest; published data include only $R/t >> 100$.

- (3) Detailed information on buckling modes and post-buckling geometry to provide guidance for the (later) development of theoretical predictions of postbuckling load-deflection characteristics possibly along lines similar to those of References 10 and 11 for lifting-surface structures.

A description of the cylindrical test specimens employed and of limited measurements made of the stress-strain properties of these specimens is given in Section II. The buckling and postbuckling experiments performed and the testing procedure employed are discussed in Section III. Section IV is devoted to a discussion of the test results for the cylindrical specimens.

SECTION II
DESCRIPTION OF CYLINDRICAL
TEST SPECIMENS AND
STRESS-STRAIN MEASUREMENTS

2.1 Cylindrical Test Specimens

Since it was believed that tests of cylindrical test specimens with radius-to-thickness ratios, R/t , ranging from about 50 to 100 would reveal those buckling and postbuckling features of primary interest for typical related structures, test specimens with nominal R/t 's of 50, 75, and 100, and a nominal length of 8 inches, were prepared from 0.065-inch wall by 2-inch O.D. stock 6061-T6 aluminum alloy tubing by chemical milling to achieve the required wall thicknesses 0.020, 0.013, and 0.010 inch, respectively. Since the chemical milling process does not diminish significantly any thickness imperfections which may exist in the original drawn tubing in some cases there were wall-thickness variations which were appreciable fractions of the mean wall thickness; the achieved mean wall thicknesses and the associated wall-thickness variations are listed in Table 1 for the 35 specimens whose failure and/or postfailure characteristics are included in this report. A "map" of the wall-thickness distribution for a typical test specimen is given in Fig. 2.

2.2 Material Stress-Strain Measurements and Results

To serve as a check on the stress-strain properties of the present materials, tensile stress-strain measurements were made using test coupons cut from each of several wall-thickness cylinders. Since selected cylinder radius-to-thickness ratios were achieved by reducing the wall thickness of the stock 6061-T6 aluminum alloy tubing by chemical milling, coupons were taken

both from the original stock and from some typical chemically-milled specimens. Tensile stress-strain properties for these specimens were measured by standard tensile tests, with strains being measured by wire-resistance strain gages.

Typical stress-strain results from these tests are shown in Fig. 1, where, as expected, the properties of the virgin material and of the chem-milled material are indistinguishable. In this figure, the tensile and compressive stress-strain diagrams for 6061-T6 tubes given in the MIL-Handbook [14] are also plotted for comparison.

SECTION III

TESTS AND PROCEDURE

In the present study, it was desired to determine the buckling and postbuckling characteristics of unstiffened cylindrical shells of various radius-to-thickness ratios under pure bending, pure axial compression, and combined bending and axial compression. To accomplish this, one test arrangement was employed for the pure bending experiments, and a second arrangement for the latter two conditions. A description of these aspects of the present test program follows.

3.1 Cylinders in Pure Bending

A schematic of the loading arrangement for testing the cylindrical specimens is shown in part (a) of Fig. 3. The actual test specimen occupies only a portion of the span between the support points, A and B, with "rigid" loading arms extending from the ends of the cylindrical model to the load-application points; the ends of the cylindrical specimen are attached to the rigid loading arms in a "fully-clamped" manner. The actual loading arrangement is shown in Fig. 4. Note that rigid reference arms were provided at each end of, and perpendicular to, the axis of the test cylinder; dial gages were positioned at the four locations shown in Fig. 4 in order to measure the total rotation between the ends of the loaded cylinder. Since the normals to these reference planes during buckling and postbuckling deformation of the cylindrical specimen do not necessarily lie in the plane of loading (that is, in the plane containing the two P loads and the axis of the undeformed cylinder), two additional dial gages were positioned diagonally to define uniquely the relative orientations of these reference planes, with a seventh dial gage measurement included to serve as an

independent check measurement. This dial-gage arrangement is shown in Figs. 4, 5, and 6.

Typically, a pure-bending test proceeded by the application of small increments of deflection-controlled loading; the use of a very stiff loading apparatus permits a careful determination of the load-deflection characteristics of the specimen, thus avoiding a large data gap immediately following buckling from which the dead-weight testing method suffers. The applied bending moment, M , and the associated dial-gage readings were recorded. After buckling of the test specimen occurred, the deflection was increased in small increments and the associated equilibrium bending moment was measured. In some cases the postbuckling load-deflection measurements were carried out with monotonically increasing deflections; in other cases, the load-deflection measurements were made during unloading to zero bending moment and subsequent re-loading at various points along the postfailure load-deflection curve; in still other cases, the unloading from the postfailure regime was carried beyond zero bending moment and reversed moment applied, with subsequent re-loading to larger of deformation values. Typical results from these tests are described in Section IV.

3.2 Cylinders under Combined Axial and Bending Loads

This loading condition is indicated schematically in part (b) of Fig. 3. The actual loading arrangement is shown in Fig. 5 with an unbuckled test specimen; this same arrangement is shown in Fig. 6 after buckling has occurred. For this type of loading, an eccentric axial compressive load was applied to the cylindrical specimen through spherical bearings using a "stiff" screw-type testing machine for fine-deflection (and load) control, in

order to investigate both incipient buckling and postbuckling behavior under various ratios of combined compressive axial load and bending moment. The distance between the bearings was decreased, and thus the load was increased, in small increments; hence, while the deflections of the cylindrical specimen remained small, the ratio of axial load to bending moment remained fixed. This ratio was changed in succeeding tests by varying the initial eccentricity $e = e_0/L$ (see Fig. 3 and Table 1). Following incipient buckling, the axial shortening was increased in small increments in order to determine the "postfailure" load-deflection characteristics under the present loading; the associated equilibrium load was measured at each step, and the deflections were measured by means of seven dial gages as described previously. These tests were usually continued to very large angular deformations of the buckled cylinder. In some cases, unloading and re-loading at various stages in the postbuckling regime were carried out, with reversed loading and re-loading in a few instances.

In summary, measured in each test were the applied external loads, applied moments, the angle between the reference planes which are located at the end of the cylinder (and which are perpendicular to the axis of the undeformed cylinder), and the angle between the plane of loading and the plane of bending. The plane of bending was determined by the pivots on the end plates of the testing machine and the geometric center of the unbuckled shell or the center of the buckled portion in the postfailure region.

SECTION IV

TEST RESULTS AND DISCUSSION

Thirty-five cylindrical specimens were tested; each of six combinations of compressive axial load and bending moment was employed with each nominal R/t shell, 50, 75, and 100. Table 1 summarizes the model characteristics and loading conditions as well as buckling load and buckling-mode data for these 35 specimens. In the following subsections, the buckling-mode features, incipient buckling conditions, and the post-buckling load-deflection characteristics of these shells are discussed.

4.1 Buckling-Mode Features

Figures 7 through 10 include photographs of 31 of the 35 specimens tested (specimens I-2, II-4, V-3, V-4, and VIII-2 are not shown). Figure 7 shows the buckled configurations of specimens subjected to pure bending. The buckled configurations of specimens with nominal $R/t = 50, 75$, and 100 subjected to combined axial compressive load and bending moment are shown in Figs. 8, 9, and 10, respectively.

Observe that an arrow is shown near an end of most of the specimens; this arrow identifies the plane of loading. An examination of the buckle patterns discloses that 30 of these specimens have symmetric and 5 have antisymmetric buckle patterns with respect to the plane of loading. The distinctive features of these two types of patterns are shown in Fig. 11. Also, it was observed that the buckle pattern consists of an interleaved 2-row pattern with a total number of peripheral half-wave-lengths at incipient buckling ranging from 4 to 14; this number tended to increase slightly as the specimen was forced to undergo

larger and larger postfailure deformations. The character of the buckling pattern, symmetric (S) or antisymmetric (A), and the number of peripheral half-wave-lengths at incipient buckling and at the end of the postbuckling test of each specimen are given in the next-to-the last column of Table 1.

A more detailed view of a typical symmetric buckle pattern is given in Figs. 12 and 13, and a typical antisymmetric buckle pattern is shown in Fig. 14.

4.2 Incipient-Buckling Results

The applied loads, pure moment or combined axial compressive load and bending moment, observed at incipient buckling are listed in Table 1 for each specimen; shown also is the maximum fiber compressive stress at incipient buckling, computed from

$$\sigma_{cr} = \frac{M_{cr} y_{max}}{I} \text{ for pure moment}$$

or

$$\sigma_{cr} = \frac{M_{cr} y_{max}}{I} + \frac{P_{cr}}{A} \text{ for combined loading}$$

Referring to the stress-strain data of Fig. 1, the 0.2 percent offset yield stress is seen to be about 40,000 psi; however, the stress-strain curve is linear up to a stress of about 32,000 psi. Examining the σ_{cr} data listed in Table 1, it is seen that incipient buckling occurred in the plastic range for all nine pure-bending-moment specimens which included $R/t = 50, 75, \text{ and } 100$. For the combined-loading tests, Fig. 15 shows the computed σ_{cr} as a function of loading eccentricity for each nominal value of R/t ; for these cases, it is seen that plastic buckling occurred

in nearly all of the cases; (linear) elastic buckling occurred in only one case.

An extensive series of tests to determine the buckling thresholds of thin-walled cylinders under combined loading has been conducted by Bruhn [2], which comprises the only large body of data on shells with R/t values as low as 200; there are results elsewhere in the literature but again pertain to R/t 's larger than the range of interest in this report. Bruhn conducted 78 tests of cylinders in combined compression and pure bending for cylinders with R/t values ranging from 230 to 800 and L/D values from 0.5 to 2.0. Figure 16 presents a summary of Bruhn's data for convenient comparison with the results of the present report.

Bruhn concluded that the R/t ratio appeared to have no significant influence on the shape of the interaction curve; the results of the present study are shown in Figs. 17, 18, and 19 and are in accord with that conclusion.

In Figs. 17, 18, and 19 the present incipient-buckling data for $R/t = 50, 75$, and 100 , respectively, are shown in terms of stress ratios as is common practice (see Refs. 2, 14, 15); that is, the incipient-buckling threshold is shown as a function of $R_c^x = P/P_o$ and $R_b^y = M/M_o$ for each R/t , where P_o is the incipient-buckling moment for pure bending. Such displays are sometimes referred to as combined-loading buckling-threshold interactions curves. It is usual to express this interaction curve in the form [14, 15]

$$R_b^x + R_c^y = 1$$

in nearly all of the cases; (linear) elastic buckling occurred in only one case.

An extensive series of tests to determine the buckling thresholds of thin-walled cylinders under combined loading has been conducted by Bruhn [2], which comprises the only large body of data on shells with R/t values as low as 200; there are results elsewhere in the literature but again pertain to R/t 's larger than the range of interest in this report. Bruhn conducted 78 tests of cylinders in combined compression and pure bending for cylinders with R/t values ranging from 230 to 800 and L/D values from 0.5 to 2.0. Figure 16 presents a summary of Bruhn's data for convenient comparison with the results of the present report.

Bruhn concluded that the R/t ratio appeared to have no significant influence on the shape of the interaction curve; the results of the present study are shown in Figs. 17, 18, and 19 and are in accord with that conclusion.

In Figs. 17, 18, and 19 the present incipient-buckling data for $R/t = 50, 75$, and 100 , respectively, are shown in terms of stress ratios as is common practice (see Refs. 2, 14, 15); that is, the incipient-buckling threshold is shown as a function of $R_c^x = P/P_0$ and $R_b^y = M/M_0$ for each R/t , where P_0 is the incipient-buckling moment for pure bending. Such displays are sometimes referred to as combined-loading buckling-threshold interactions curves. It is usual to express this interaction curve in the form [14, 15]

$$R_b^x + R_c^y = 1$$

where the exponents x and y are determined experimentally for the particular compressive-member geometry and material properties involved. Shown as a dashed line in each of Figs. 17, 18, and 19 for convenient comparison is the above stress-ratio equation where both x and y are taken as unity; the present data are too sparse to permit determining a valid interaction equation of the type discussed above. For convenient reference, the data points on Figs. 17, 18, and 19 are each accompanied by a number in brackets, which represents the total number of peripheral half-wave lengths of the buckle pattern at incipient buckling.

From Figs. 7 through 10 it is seen that in several tests the buckling pattern occurred near the end of a specimen; however, in attempted repetitions of such tests, the buckling pattern occurred well away from the end of the specimen. The incipient buckling load for such cases, as shown in Table 1, was nearly identical. Also, for specimens of given nominal wall thickness, it was found that the wall-thickness variations in the present specimens did not affect significantly either the incipient-buckling load or the features of the buckling mode. Furthermore, the occurrence of an antisymmetric rather than a symmetric buckling pattern for a given R/t and loading condition did not affect the critical buckling load significantly; this can be seen, for example, by comparing the results of tests 5, 6, and 7 or of test 14 with 16 in Table 1.

4.3 Postbuckling Load-Deflection Characteristics

Both the prebuckling and the postbuckling load-deflection characteristics of the present cylindrical shells, in the case of pure bending, may be described conveniently in terms of the measured bending moment, M , as a function of the angle, θ ,

between the reference planes positioned at the ends of and perpendicular to the axis of the undeformed cylinder. As depicted in Fig. 20, this total angle of rotation θ consists of elastic contributions (θ_2 and θ_3) from the unbuckled portion of the specimen plus a (usually much larger) contribution θ_1 from the spanwise region bounding the buckled portion. It is this contribution (θ_1) which is of primary interest for postbuckling dynamic response analysis purposes.

For the cylinders under combined loading, the applied axial load P and the associated axial shortening $b-c$ due to buckling (of the buckled length) are parameters of interest in addition to the $M-\theta$ behavior. In the postfailure range, the contribution of elastic shortening of the unbuckled portion is small, and the effect is, qualitatively, the same as the elastic contribution to the bending angle in the pure-moment case discussed above.

The remaining measured quantity of interest is the angle between the plane of loading and the plane of bending. Although the cylinders were loaded in a consistent fashion, the plane about which buckling (either symmetric or antisymmetric) occurred did not coincide, in general, with the loading plane. The plane defined by the center of the buckled portion of the shell, and the loading points of the test machine is defined as the "plane of bending"; whereas the plane defined by points A, B, and C of Fig. 20 is defined as the "plane of loading". An assessment of the measurements from the present experiments shows this angle to be small -- not exceeding 10 degrees, and being generally less than 4 degrees. In view of these small values, the effect of this angular "error" results in negligible changes to the "uncorrected" load-deflection characteristics of the present test specimens.

Typical load-deflection characteristics of the present specimens for both the elastic and the postbuckling regime are illustrated in Fig. 21. It is seen that a near-linear load-deflection curve is obtained until buckling occurs. Following buckling, the load-carrying ability (either M or P) of the structure drops sharply. As the deflection is increased monotonically, M or P decreases monotonically until the deformation becomes so large that binding or mutual-support between adjacent elements in the buckled portion occurs; at this point, the load-supporting ability of the structure increases with increasing deflection. Note also that if the structure is unloaded from some condition in the postbuckling range, the associated so-called "pseudo-elastic" load-deflection path is nearly linear but has a slope somewhat less than that for the prebuckled structure; upon re-loading, the load-deflection path becomes slightly steeper than that for unloading and then rejoins the "main postbuckling curve", exhibiting a small hysteresis loop. Unloading from a larger postbuckling value of deflection leads to pseudo-elastic paths of smaller slope.

From the standpoint of postbuckling dynamic-response analysis, the structural characteristics of primary utility and interest are moment-angle and/or the axial load as a function of the axial shortening relation for the buckled portion of the span or length of the structure; these characteristics are termed herein $M-\theta_1$ and $P-\delta_1$ relations, respectively. Note that in the present experiments, the overall angular deflection θ and the overall axial shortening δ for the entire test specimen of length L were measured, whereas the corresponding values for the buckled portion, b, of the specimen are of ultimate concern.

An inspection of part (a) of each of Figs. 20 and 21 shows that at any given point Q in the postbuckling range, the moment-carrying ability of the buckled section is M_Q , and the associated angular rotation $\theta_{1,Q}$ of the buckled portion of the test specimen is given, to a good approximation, by

$$\theta_{1,Q} = \theta_Q - \frac{b}{L} \theta_{e,Q}$$

where $\theta_{e,Q}$ is the total relative angular end-plane rotation of the entire specimen in the prebuckling region at an applied bending moment M_Q . Thus, with the overall M-θ characteristics and the buckle-zone length b (see Table 1) given, the desired $M-\theta_1$ data can be determined readily. Figures 22 and 23 illustrate typical M-θ and $M-\theta_1$ characteristics for specimens with R/t values of 50 and 75, respectively, and which were subjected to pure-moment loading. For specimens with R/t values of 100, the postbuckling M-θ characteristics are not available since buckling occurred near the end of the shell, and bending with the shell mounting began immediately upon further loading.

Referring to part (b) of each of Figs. 20 and 21, it is seen that, for the case of combined loading, similar remarks to the preceding also apply with respect to the associated M-θ characteristics and the P-δ characteristics, with the following modifications. First, for small deflections of an eccentrically-loaded specimen, the bending moment at the critical station is given by $P \cdot e$; however, as the structural deflection increases, the moment arm to the critical station increases and the correct bending moment at that station is given by $P \cdot e_1$. Again, the effective relative end rotations θ_1 for the buckled-length portion b of the specimen can be obtained from the measured

overall relative-end-rotation for the entire test specimen. Similarly, the relation between the axial compressive load P and the axial shortening δ_1 for the buckled portion, b , of the specimen can be found from the measurements made directly for P and the overall axial shortening δ of the entire test specimen. For example, δ_1 associated with any point V on the main postbuckling curve is given, to a good approximation, by

$$\delta_{1,V} = \delta_V - \frac{b}{L} \delta_{e,V}$$

where $\delta_{e,V}$ is the total axial shortening of the entire cylindrical test specimen in the prebuckling region under an applied axial compressive load P_V .

Postfailure load-deflection data including $M-\theta_1$, $P-\delta$, and $P-\delta_1$ are given in Fig. 25 for a typical specimen with an $R_t = 50$ and a nominal loading eccentricity* $e = e_o/L = 0.016$; similar data are shown in Fig. 26 for a specimen with $R/t = 50$ and $e = 2.0$. Similar typical data are shown in Figs. 27, 28, 29 and 30 for $(R/t, e)$ pairs, $(75, 0.125)$, $(75, 0.25)$, and $(100, 0.25)$, respectively.

Postbuckling data for $(R/t, e)$ pairs $(50, 0)$, $(75, 0)$, and $(100, 0)$ were not found, since for these combinations, buckling occurred near the end of the shell and binding with the shell mounting began immediately.

- - - - -
* These eccentricities could be considered in dimensionless form if desired.

The load-carrying capacity for pure bending is defined by the $M-\theta$ and the $M-\theta_1$ curve. Whereas, for combined bending and axial loading, both load-shortening and moment-rotation must be considered together. Examination of the loads carried by the shells under combined loading shows that in no case do these loads exceed maximum loads defined for that shell. Thus, the jump after buckling to a "higher" moment-carrying level in Figs. 24 and 26 is not surprising, and the rise is attributable to the sudden increase in the distance of the buckle center from the line of action of the load.

Comparing the $M-\theta_1$ results of Fig. 22 with those of Figs. 25 and 26 all of which pertain to specimens with $R/t = 50$, it is seen that axial-loading effects upon the $M-\theta_1$ behavior are not significant. A similar observation holds for the specimens with $R/t = 75$ and 100.

It is believed that the typical failure and postfailure data included provide sufficient detail so that meaningful comparisons can be made with theoretical methods which may be developed in the future to predict the postfailure characteristics of these structures.

REFERENCES

1. Timoshenko, S. and Gere, J.M. "Theory of Elastic Stability." Second Edition, McGraw-Hill Book Co., Inc., New York 1961.
2. Bruhn, E.F. "Tests on Thin-Walled Celluloid Cylinders to Determine the Interaction Curves Under Combined Bending, Torsion, and Compression or Tension Loads." NACA TN 951, 1945.
3. Gerard, G. and Becker, H. "Handbooks of Structural Stability, Part III -- Buckling of Curved Plates and Shells." NACA TN 3783, August 1957.
4. Holmes, M. "Compression Tests on Thin-Walled Cylinders." Aero. Quarterly, 12, pp. 150-164, May 1961.
5. Peterson, J.P., Whitley, R.D. and Deaton, J.W. "Structural Behavior and Compressive Strength of Circular Cylinders with Longitudinal Stiffening." NASA TN D-1251, May 1962.
6. Collected papers on "Instability of Shell Structure -- 1962". NASA TN D-1510, December 1962.
7. Thielemann, W.P. "On the Postbuckling Behavior of Thin Cylindrical Shells." NASA TN D-1510, p. 203, December 1962.

8. Gerard, G.E. "Elastic and Plastic Stability of Orthotropic Cylinders." NASA TN D-1510, p. 277, December 1962.
9. D'Amato, R. "Destruction Tests of Aircraft Structural Components. Part 1 -- Description of Static Test Techniques and Presentation of Postfailure Structural Characteristics of Some Complex Built-Up Structures." WADC TR 54-385, Part 1, June 1955.
10. D'Amato, R. "Static Postfailure Characteristics of Multi-web Beams." WADC TR 59-112 (ASTIA 211033), February 1959.
11. D'Amato, R. "Postfailure Behavior of Aircraft Lifting Surface Structures." ASD-TR-61-136, June 1962.
12. Gewehr, H.W. "Postfailure Studies of Aircraft Wing Structures." S.M. Thesis, Massachusetts Institute of Technology, Department of Aeronautics and Astronautics, 1958.
13. Stephenson, W.B. and Ripperger, E.A. "Static Failure of an Aircraft-Type Beam." Sandia Corporation, SC-4128(TR), October 1957.
14. Anon. "Metallic Materials and Elements for Flight Vehicle Structures." MIL-HDBK-5, Department of Defense, (U.S. Government Printing Office), Washington, D.C., August 1962.
15. Peery, David J. "Aircraft Structures." Ch. 8, McGraw-Hill Book Co., Inc., 1950.

TABLE 1

Summary of Test Data

Test Number	Specimen Number	Cylinder Dimensions				Loading			P_{cr} (lbs.)	M_{cr} (in.-lbs.)	Max. Stress at Buckling σ_{cr} (psi)	Buckling Mode X-Y-Z	Estimated Length of the Buckling Zone, b (in)
		Nominal (inch)	Variation (percent)	R/t	Nominal	Actual	Pure Moment	Combined, with	θ_0 (in.)	α			
1	I-1	.020	16.4	50	49.7	x	-	-	-	2875	51.2	3-S-5	1.50
2	I-2	.020	17.0	50	49.6	x	-	-	-	2815	50.1	3-S-5	1.50
3	II-1	.020	9.3	50	49.3	x	-	-	-	2815	50.1	3-S-5	1.50
4	II-3	.020	7.0	50	50.0	x	-	-	-	2800	49.8	3-S-5	1.13
5	I-3	.013	21.0	75	76.3	x	-	-	-	1645	45.6	5-S-7	1.13
6	I-4	.013	29.0	75	74.6	x	-	-	-	1650	45.7	4-A-7	1.13
7	I-6	.013	23.0	75	76.9	x	-	-	-	1645	45.6	5-A-5	1.06
8	II-2	.010	11.6	100	97.1	x	-	-	-	1185	42.6	3-S-5	1.25
9	II-4	.010	24.0	100	101.1	x	-	-	-	1185	42.6	3-S-5	1.19
10	IV-2	.020	6.9	50	49.0	-	0	0	4980	6	41.1	5-S-	-
11	VI-2	.020	8.8	50	49.5	-	0	0	5080	6	41.8	5-A-6	1.44
12	VII-1	.020	6.9	50	48.5	-	0	0	4980	6	41.1	-S-	-
13	VIII-1	.020	5.0	50	49.5	-	.125	.016	4180	536	43.9	5-S-6	1.31
14	V-9	.020	6.0	50	50.0	-	.33	.041	3170	1074	45.2	-S-5	-
15	VII-4	.020	6.9	50	49.3	-	.33	.041	3405	1149	48.5	4-S-7	1.13
16	V-6	.020	7.5	50	49.2	-	.33	.041	3190	1040	45.4	-A-7	1.13
17	VI-1	.020	4.5	50	49.5	-	.75	.094	2320	1767	50.5	-S-	-
18	VII-3	.020	6.0	50	49.8	-	.75	.094	2220	1699	48.6	3-S-7	1.31
19	IV-1	.020	7.8	50	48.8	-	2.00	.25	1125	2293	50.1	3-S-5	1.25
20	V-1	.020	8.6	50	49.3	-	2.00	.25	1035	2110	46.1	3-S-5	1.25
21	V-2	.020	5.0	50	50.0	-	2.00	.25	1085	2204	48.2	3-S-7	1.19
22	VI-9	.013	8.3	75	76.9	-	0	0	2900	0	36.9	14-S-	0.81
23	VI-7	.013	13.7	75	75.7	-	.125	.016	2460	315	40.0	9-S-	0.88
24	VII-5	.013	12.2	75	76.3	-	.125	.016	2620	336	42.5	8-S-8	1.06
25	V-6	.013	10.5	75	76.9	-	.125	.016	2470	321	40.1	7-S-	.96
26	VII-2	.013	7.6	75	75.2	-	.33	.041	2030	786	44.7	6-S-	1.00
27	VII-6	.013	9.9	75	76.3	-	.75	.094	1237	937	41.6	5-S-7	1.13
28	VIII-2	.013	8.6	75	76.3	-	.75	.094	1180	896	39.6	5-S-7	1.38
29	V-3	.013	6.9	75	76.9	-	2.00	.25	635	1286	43.7	5-S-7	1.50
30	V-8	.010	9.9	100	99.6	-	0	0	1850	10	30.8	14-A-	0.75
31	VI-10	.010	14.7	100	94.3	-	.125	.016	1800	230	37.9	12-S-	0.75
32	VII-7	.010	16.8	100	91.7	-	.33	.041	1375	462	39.2	7-S-8	0.88
33	VI-3	.010	12.7	100	99.0	-	.75	.094	900	692	39.5	6-S-9	1.00
34	V-5	.010	12.0	100	100.0	-	2.00	.25	419	843	37.7	S-9	1.00
35	V-7	.010	11.0	100	100.0	-	2.00	.25	406	817	36.0	7-S-	1.00

Explanation of Column Headings

Spec. No.: All test specimens with same Roman numeral were taken from the same tubular stock

P_{cr} : Critical buckling load in pounds

Variation of Thickness: Maximum percentage variation of shell thickness in region of buckling, measured with respect to the nominal thickness

M_{cr} : Critical buckling moment in inch-pounds

Loading: Type of loading: M = pure moment; otherwise, eccentricity of load is given for combined-loading cases

σ_{cr} : Maximum stress at buckling in psi.

Buckling Mode: First No.(X): Number of circumferential half wavelengths at initial deformation

Letter(Y): S = Symmetric buckling mode

A = Antisymmetric buckling mode

Second No.(Z): Number of circumferential half wavelengths at completion of test (See Fig. 11)

A blank at any place in the sequence indicates that information is not available.

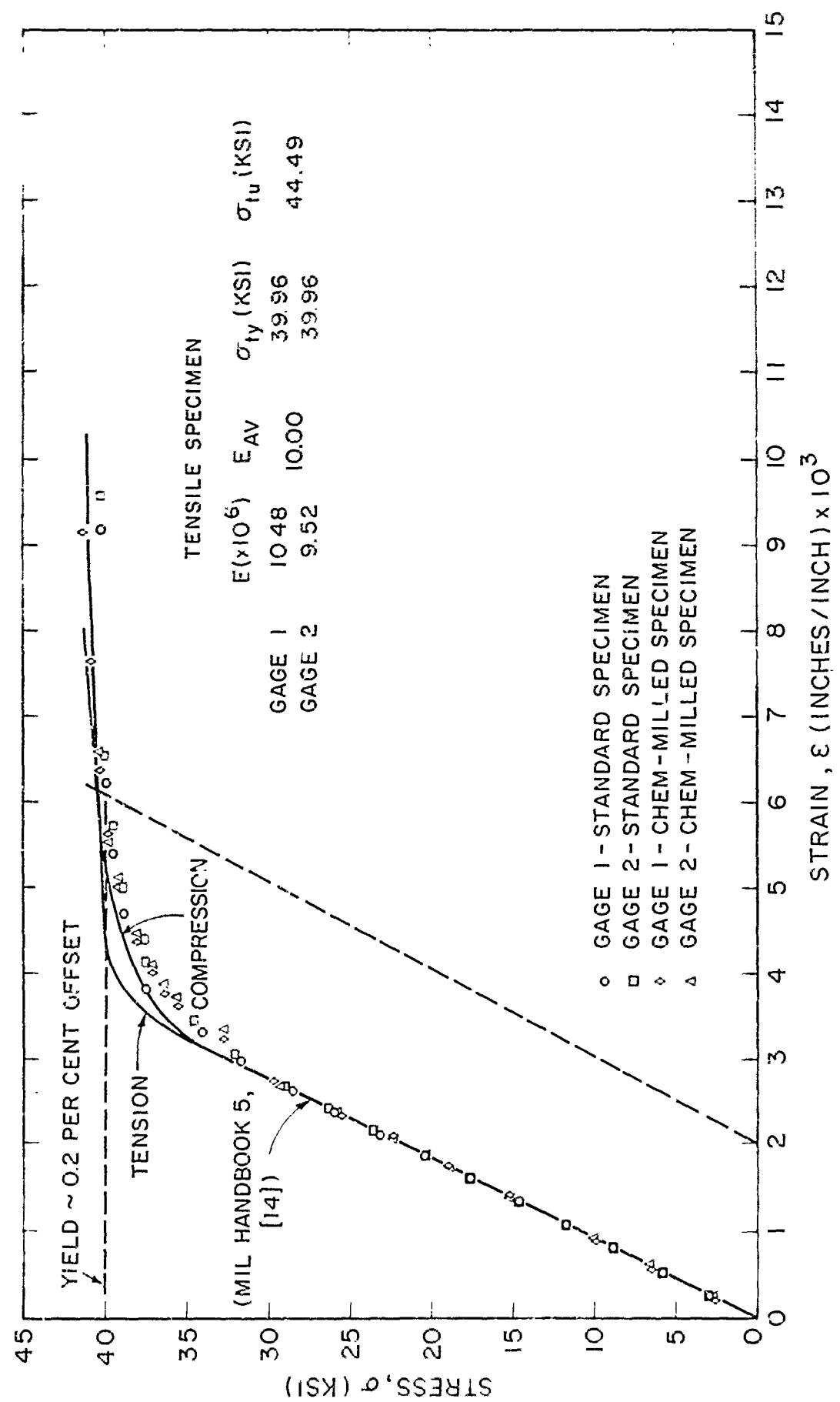


Fig. 1 Material Stress-Strain Measurements

SPECIMEN VI - 3

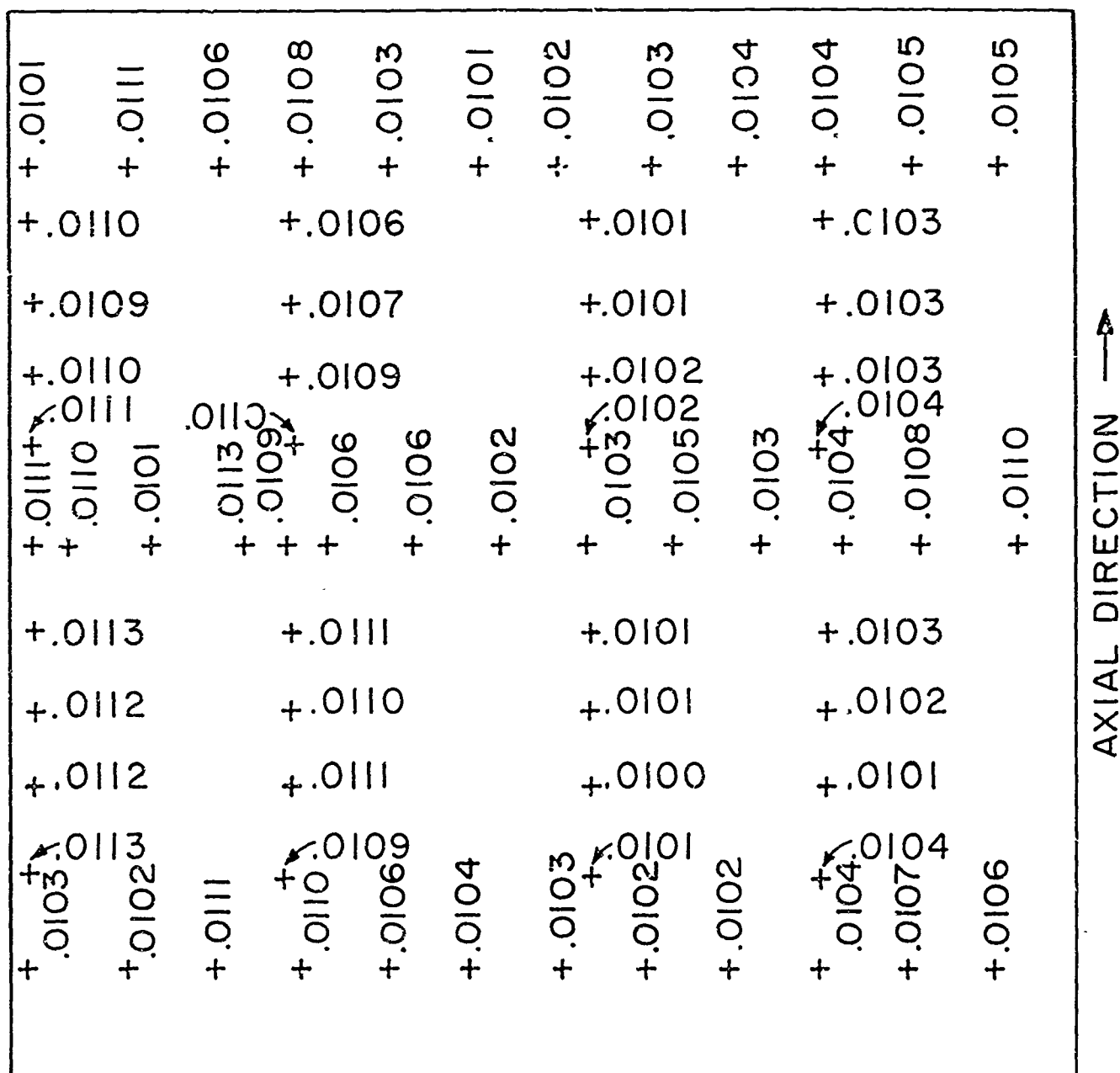
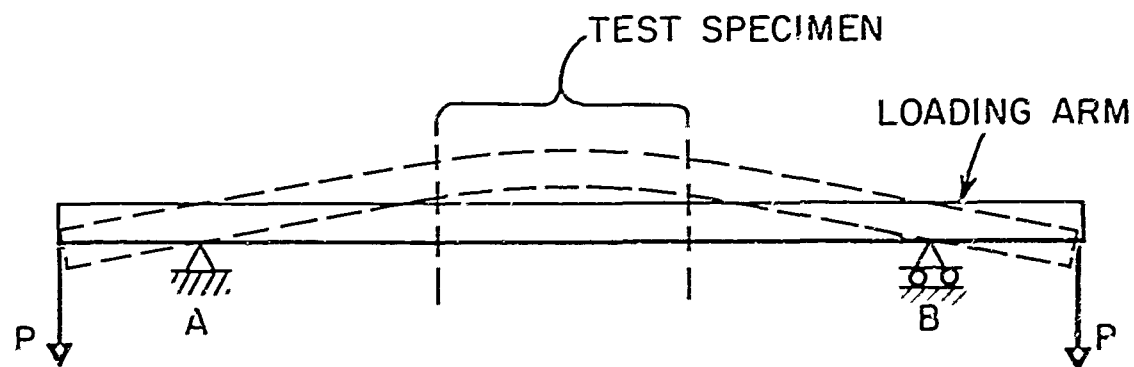
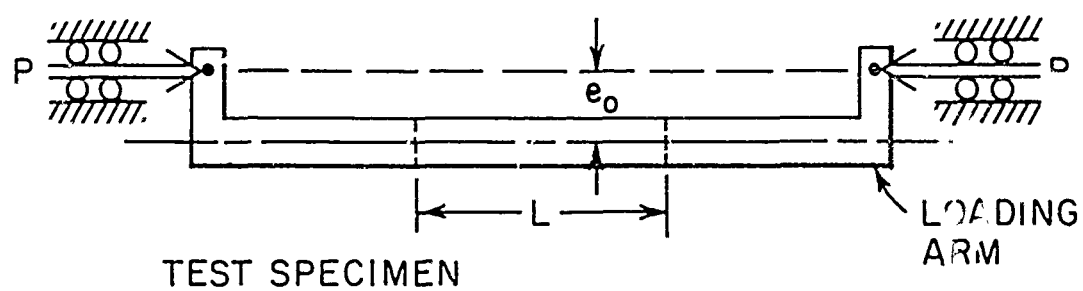


Fig. 2 Illustration of Typical Shell Wall Thickness Distribution for a Specimen with $R/t = 100$

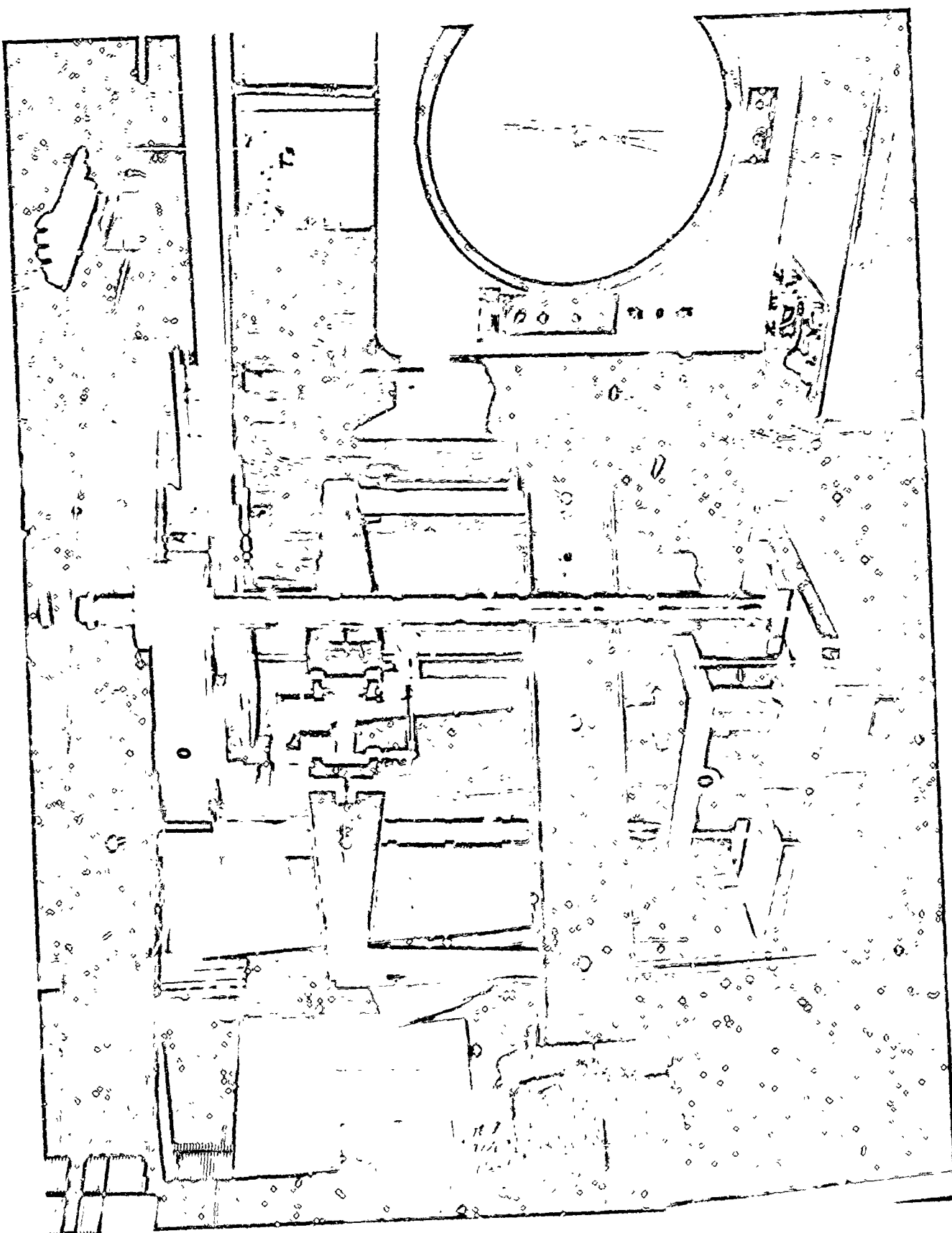


(a) Pure Bending Tests



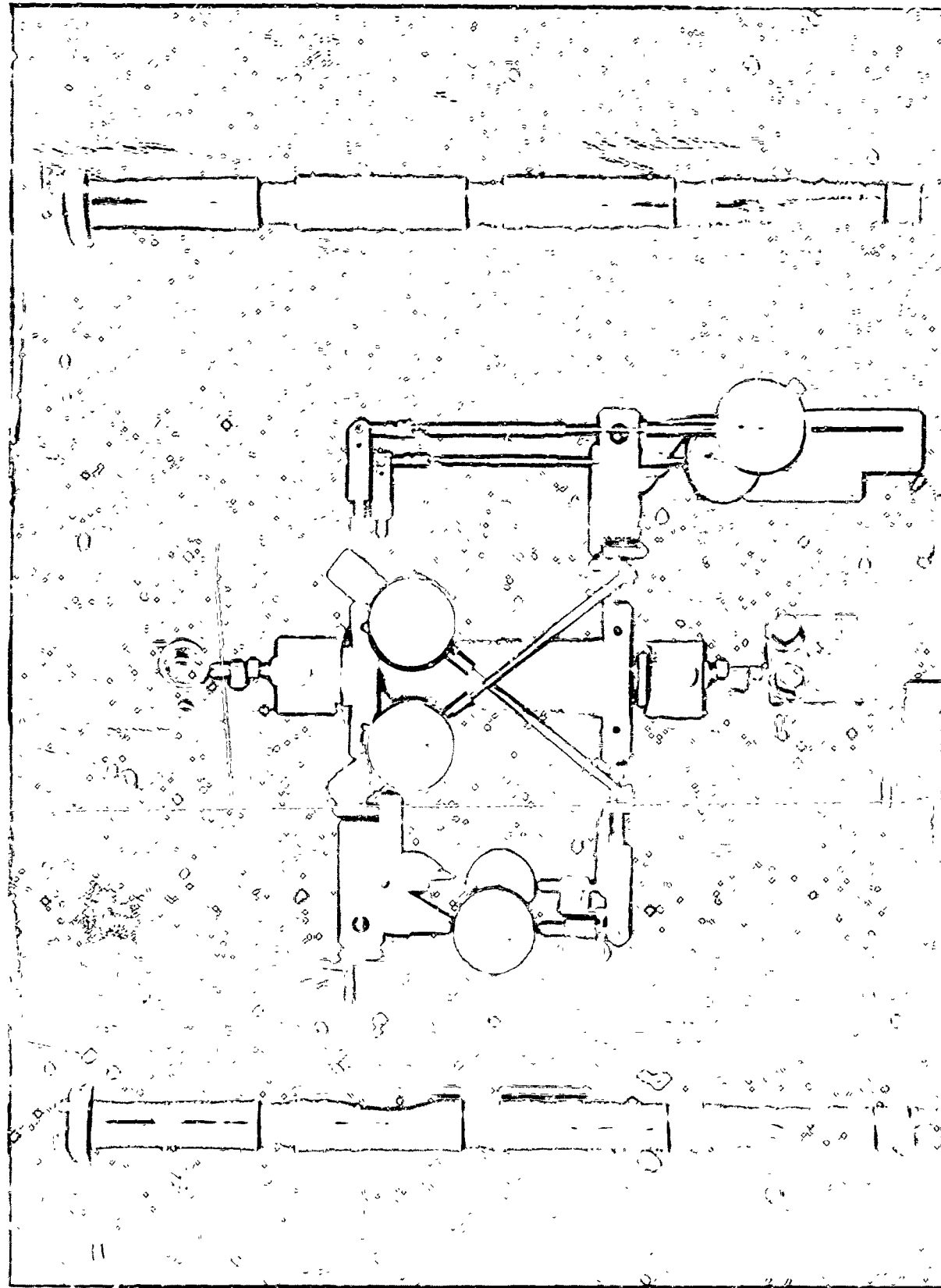
(b) Combined Axial Load and Bending

Fig. 3 Loading Schematics and Nomenclature.

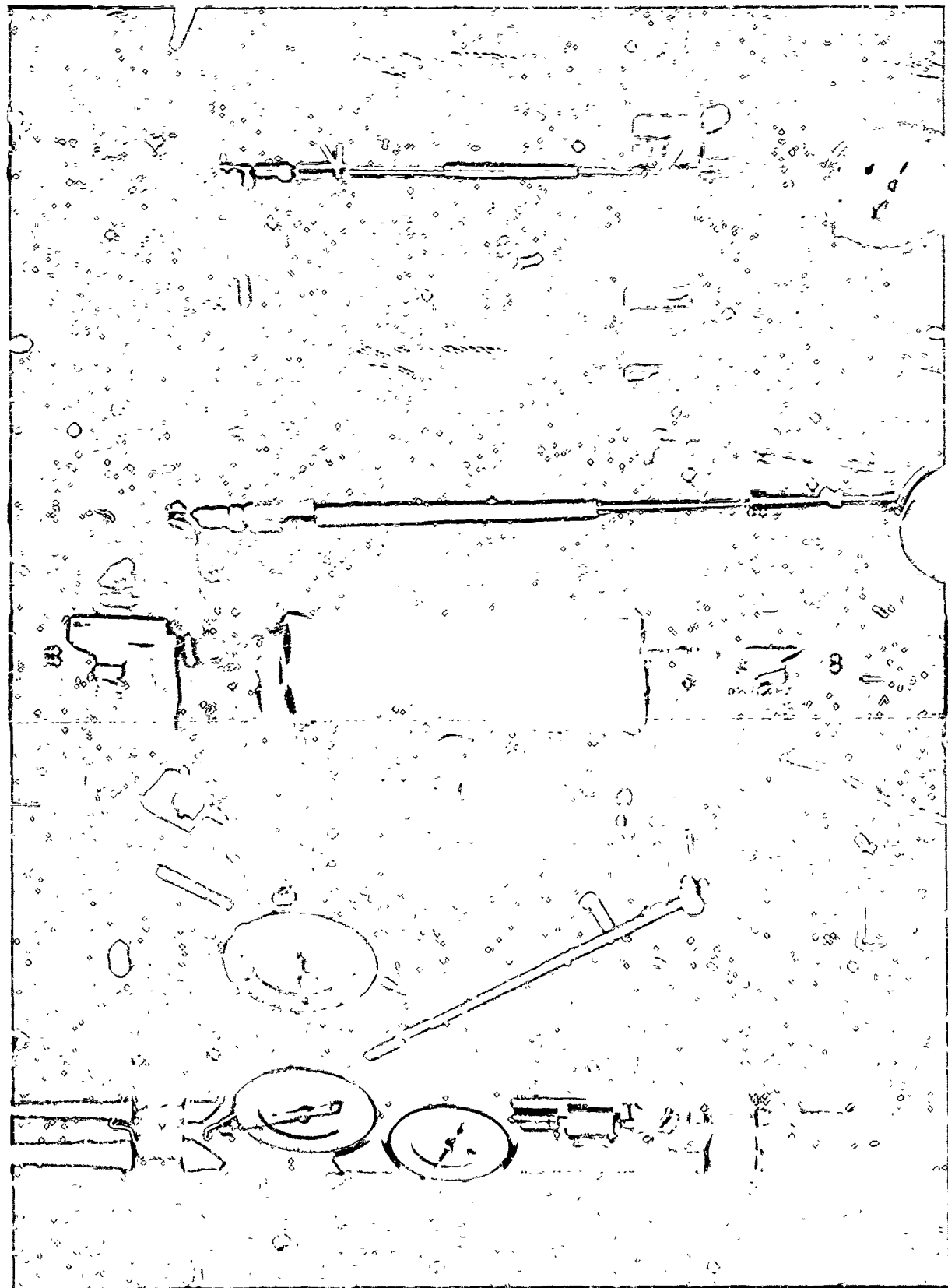


12. 4 Load Arrangement for Impact Tests

F: Test u. n. ent ing



ng Test
imen



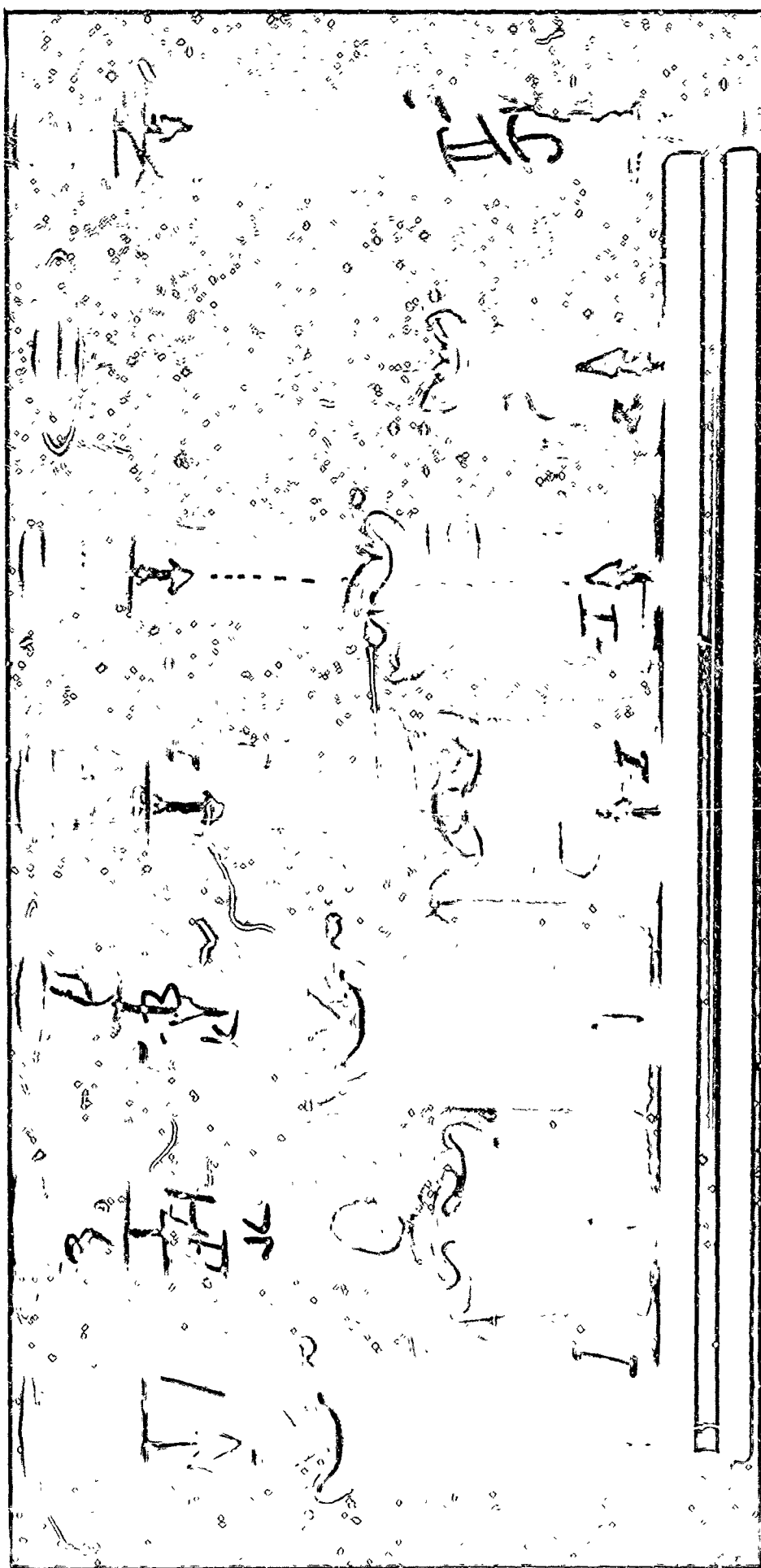


Fig. 7 Buckled Cylindrical Shells from Pure Bending Tests (Series I and II)

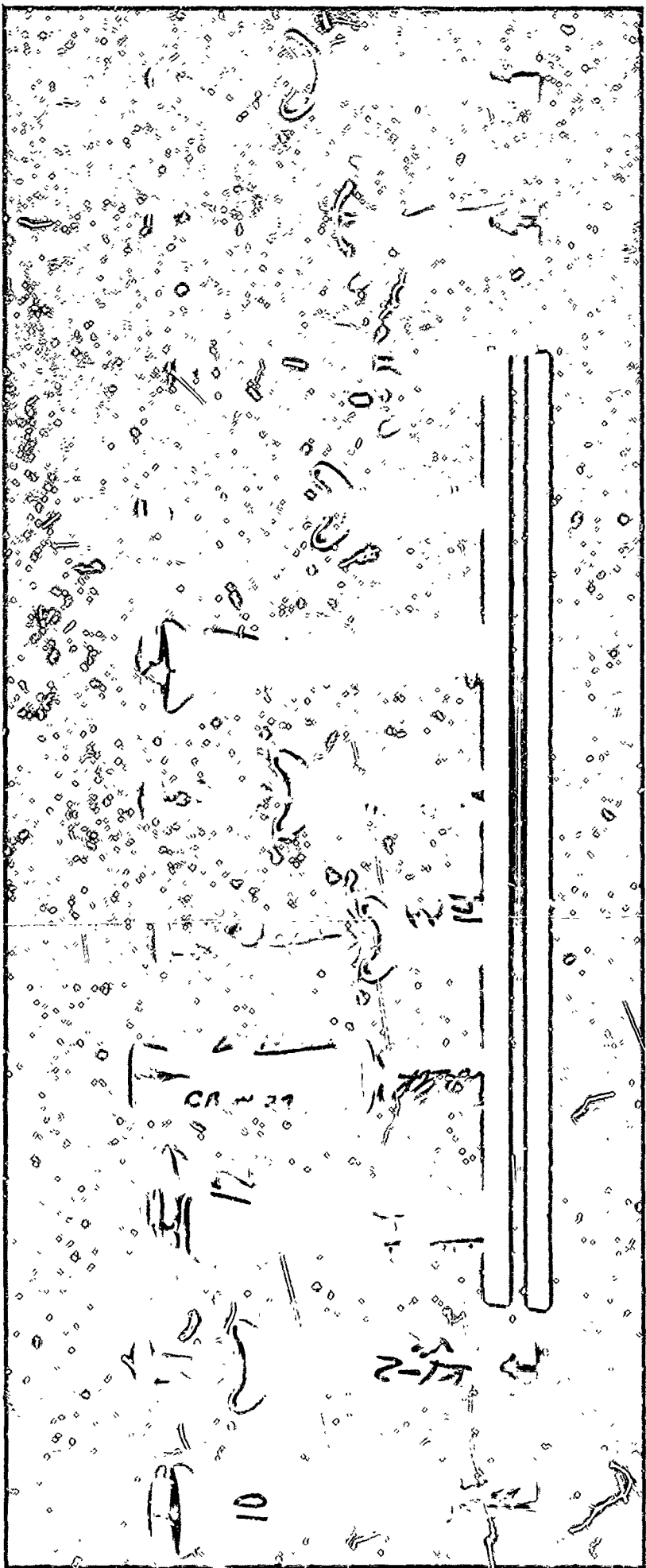


Fig. 8 Buckled Cylindrical Shells from Combined-Loading Tests, $R/t = 50$

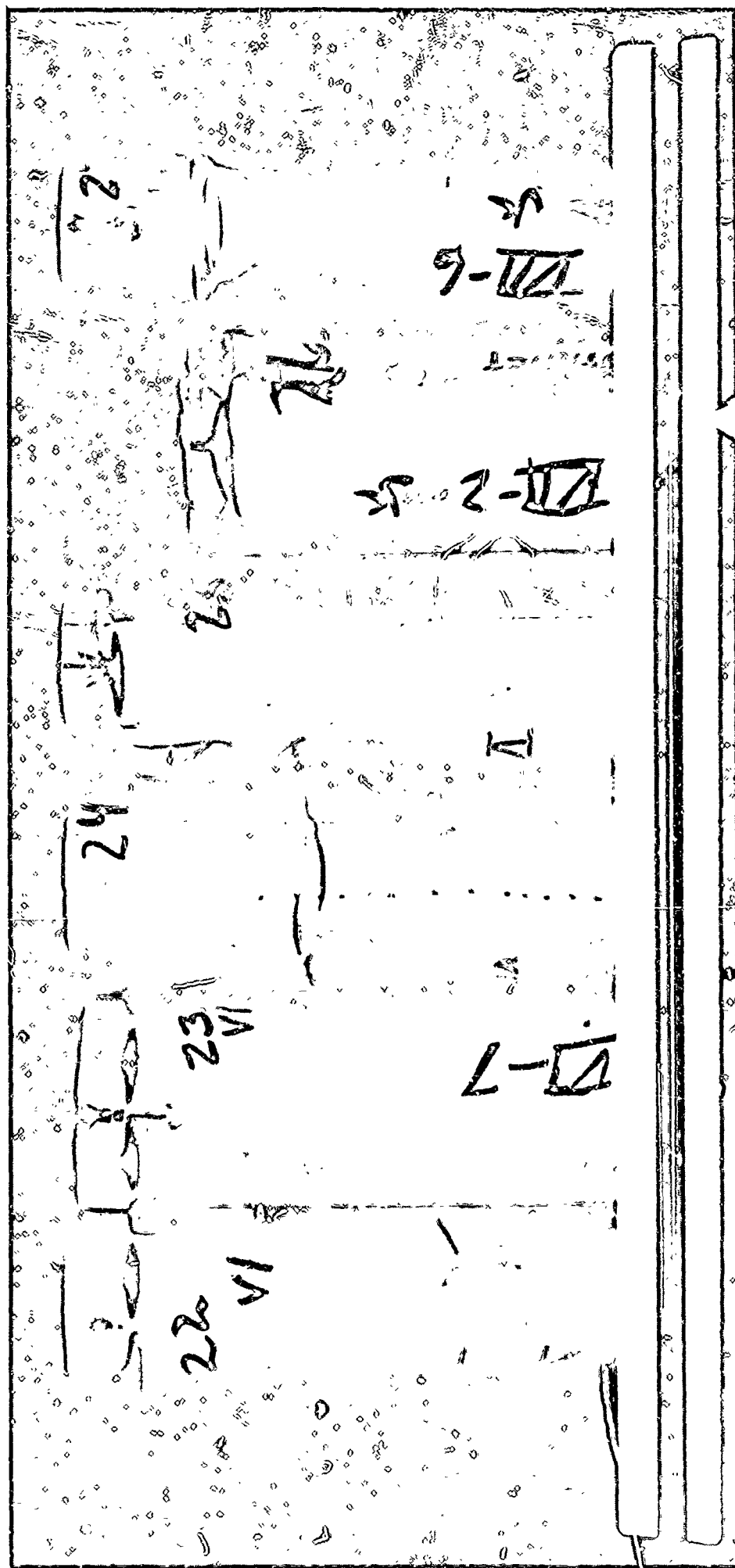


Fig. 9 Buckled Cylindrical Shells from Combined-Loading Tests, $R/t = 75$

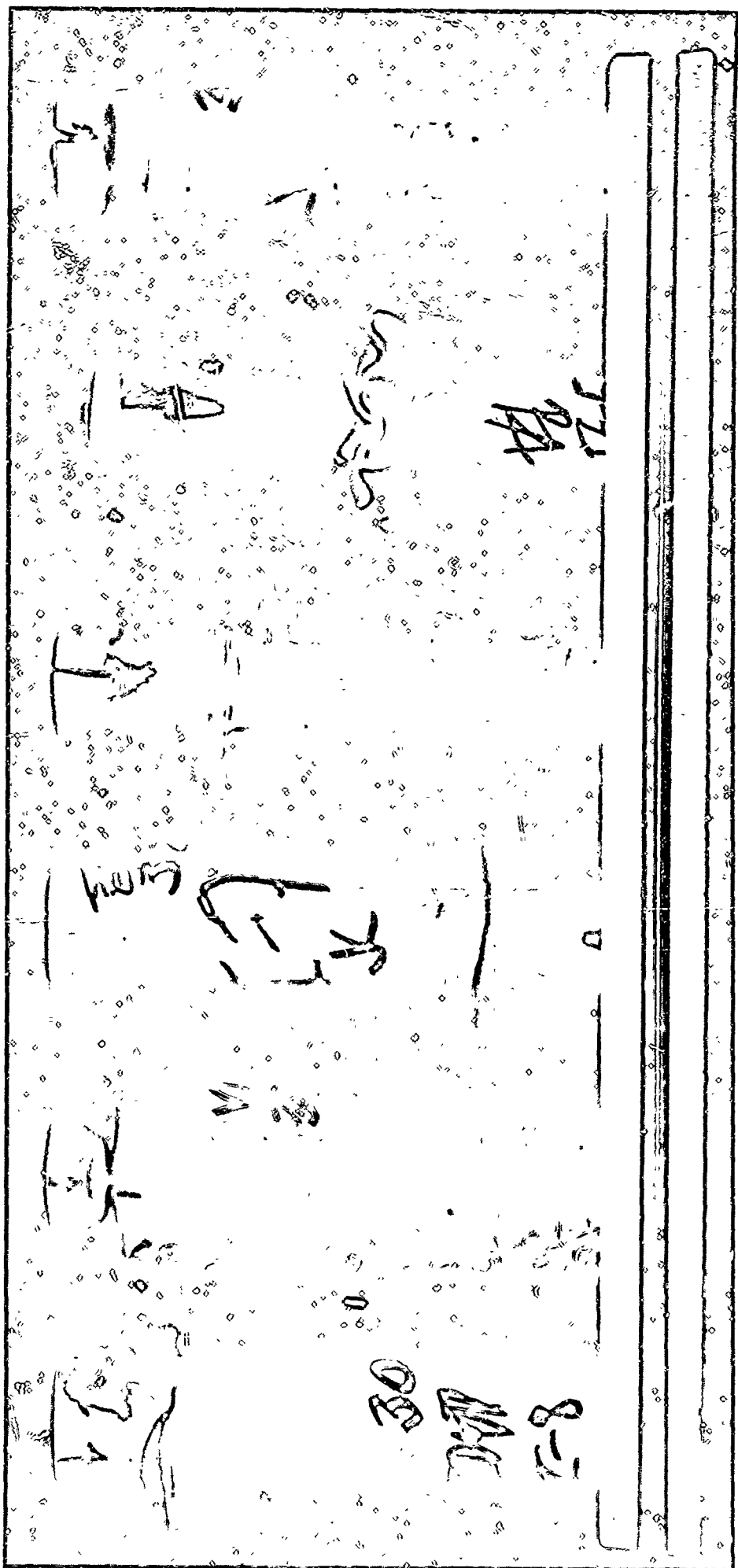


Fig. 10 Buckled Cylindrical Shells from Combined-Loading Tests,
 $R/t = 100$

◊ CONVEX REGION
X CONCAVE REGION

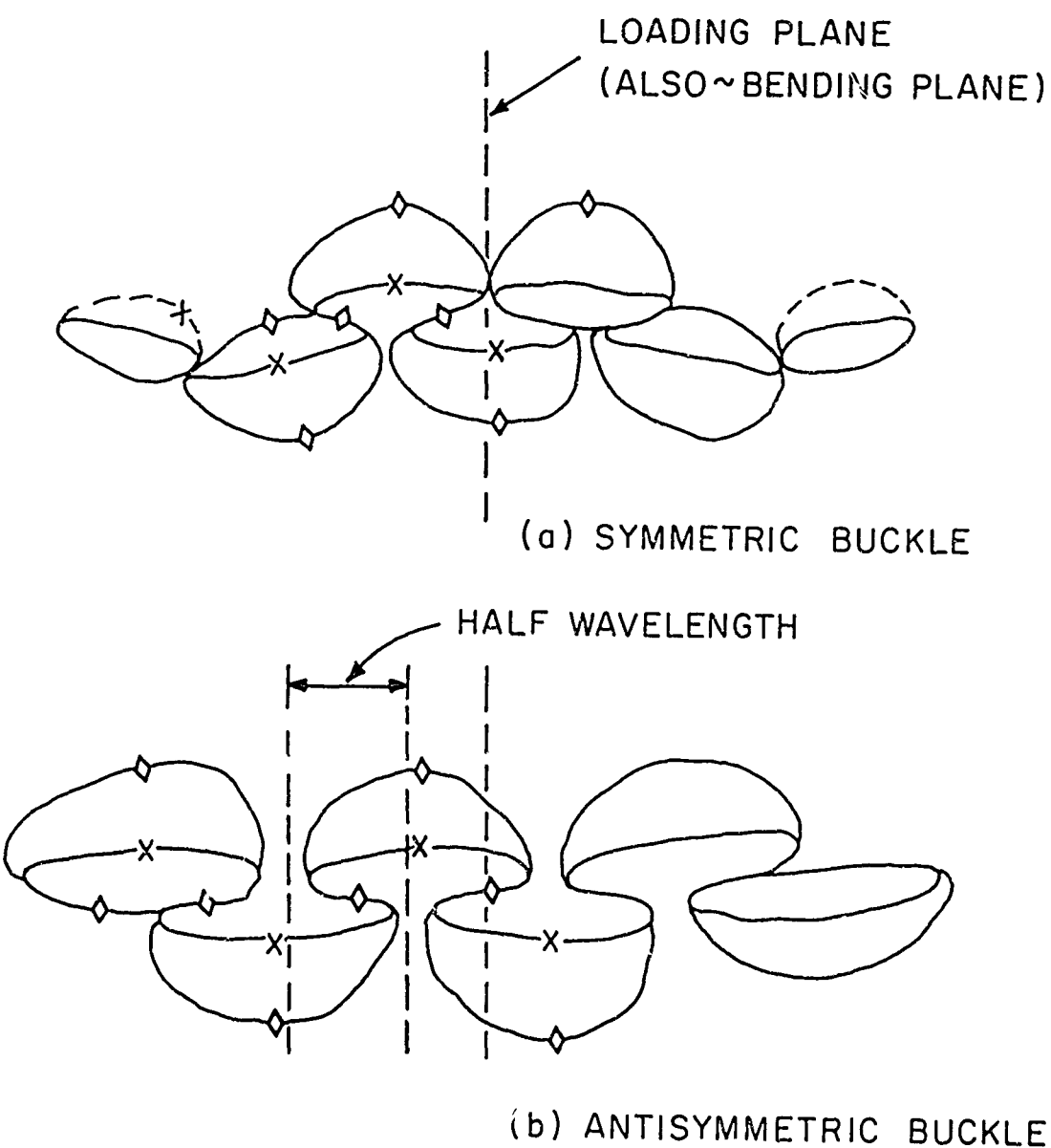


Fig. 11 Illustration and Nomenclature for Symmetric and Antisymmetric Buckle Patterns

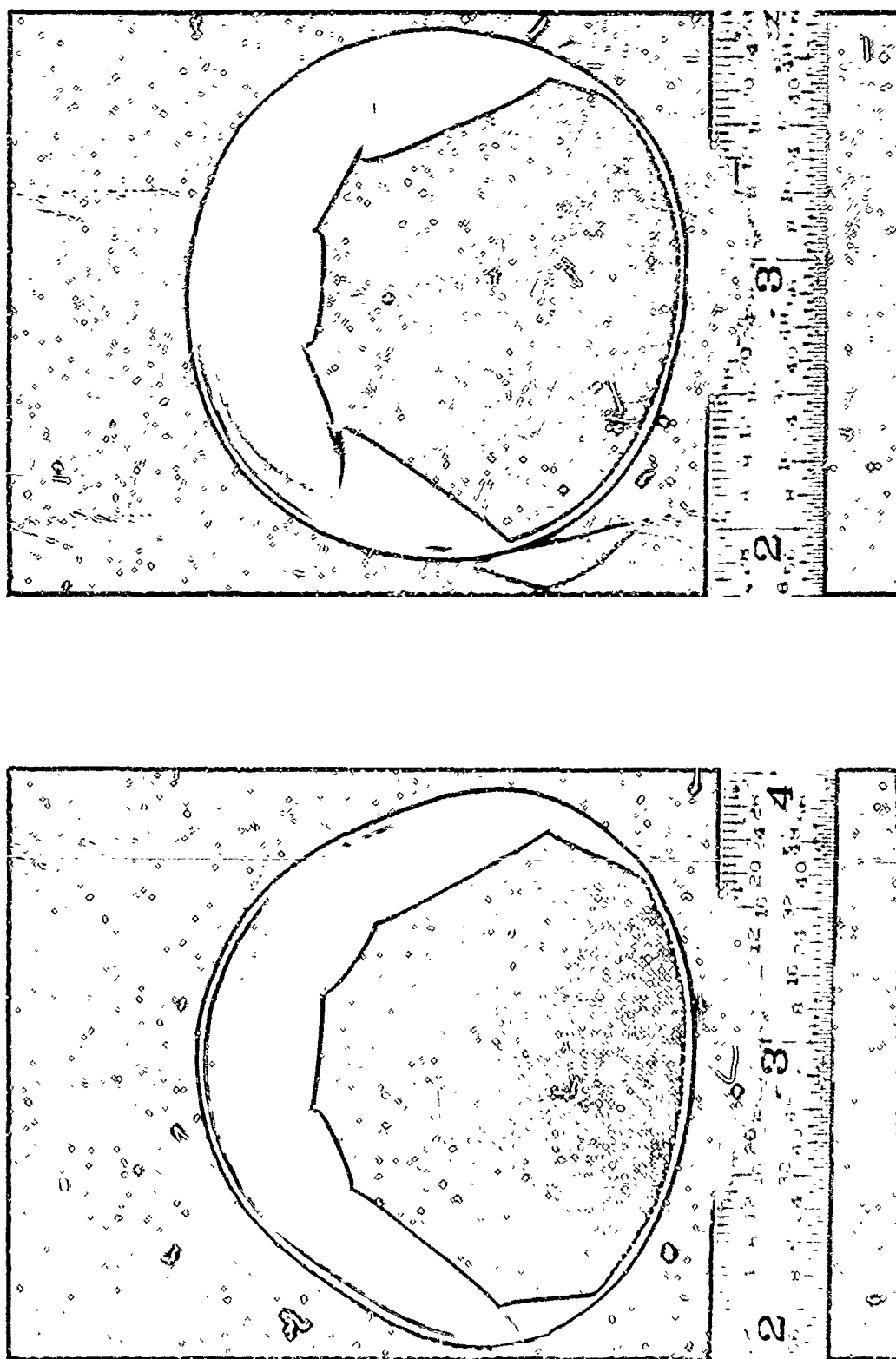


Fig. 12 Overall Section View of Shell Buckled in the Symmetric Mode, Specimen V-3

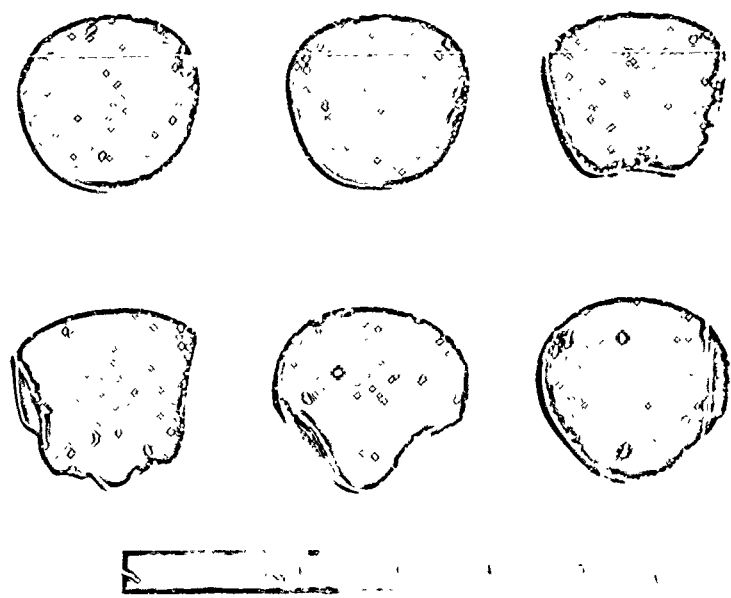
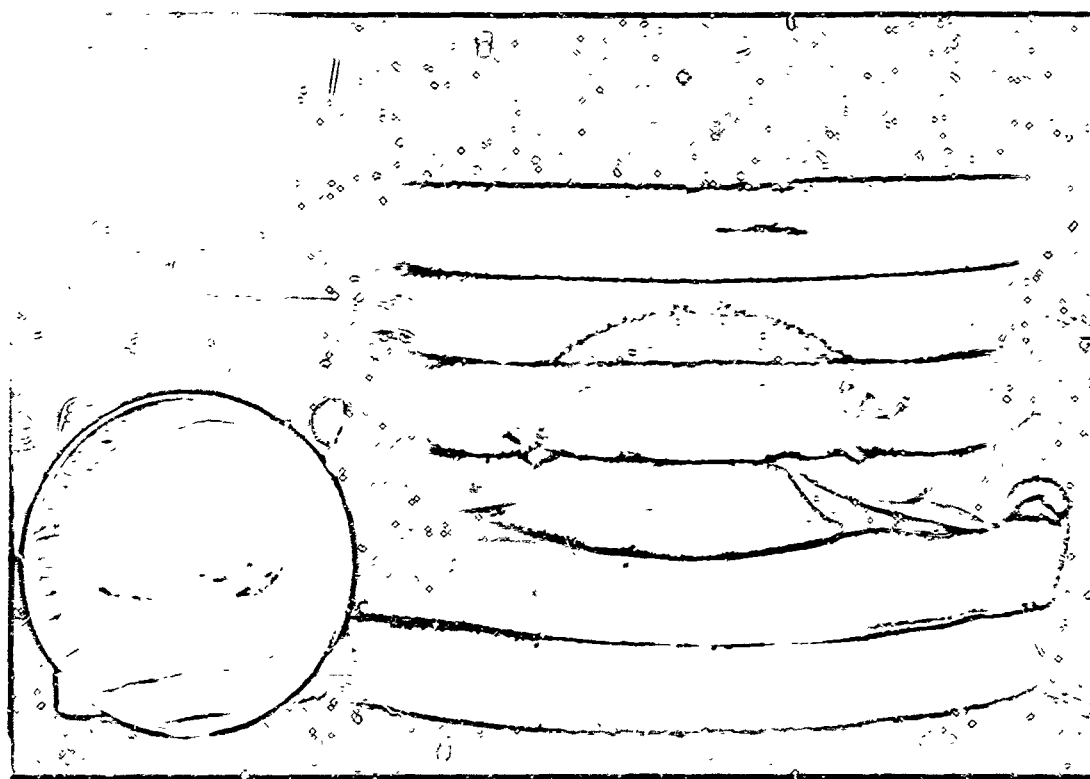


Fig. 13 Sectioned View of a Symmetric Buckle,
Specimen V-3

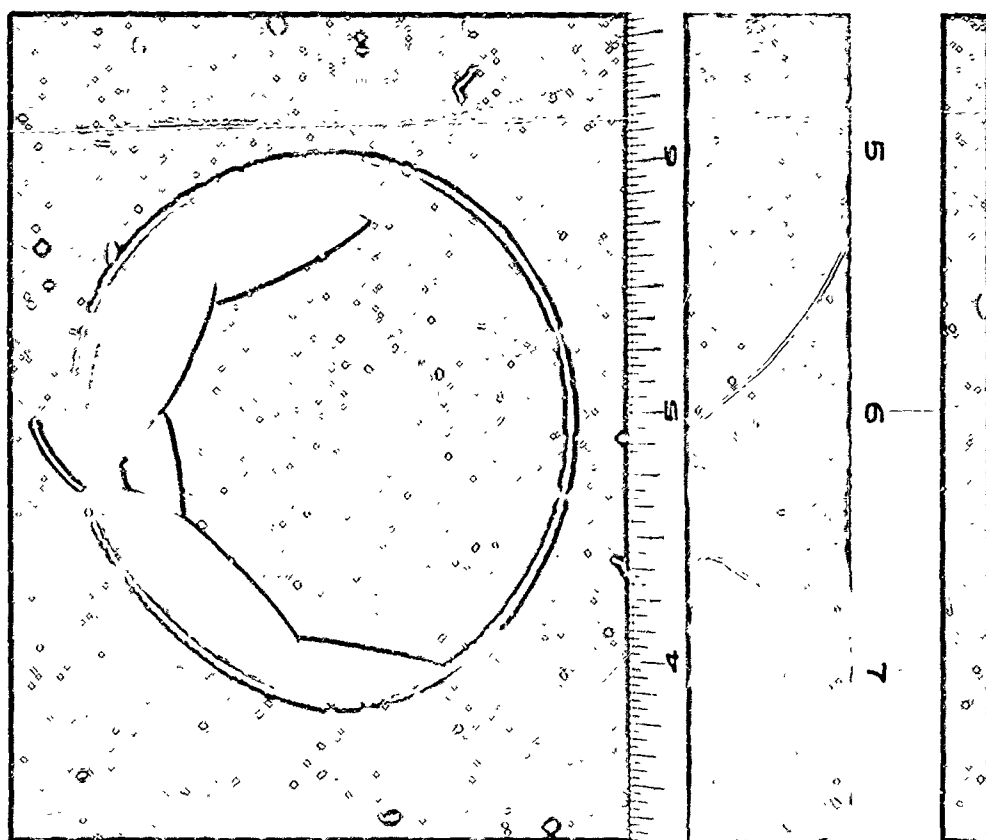
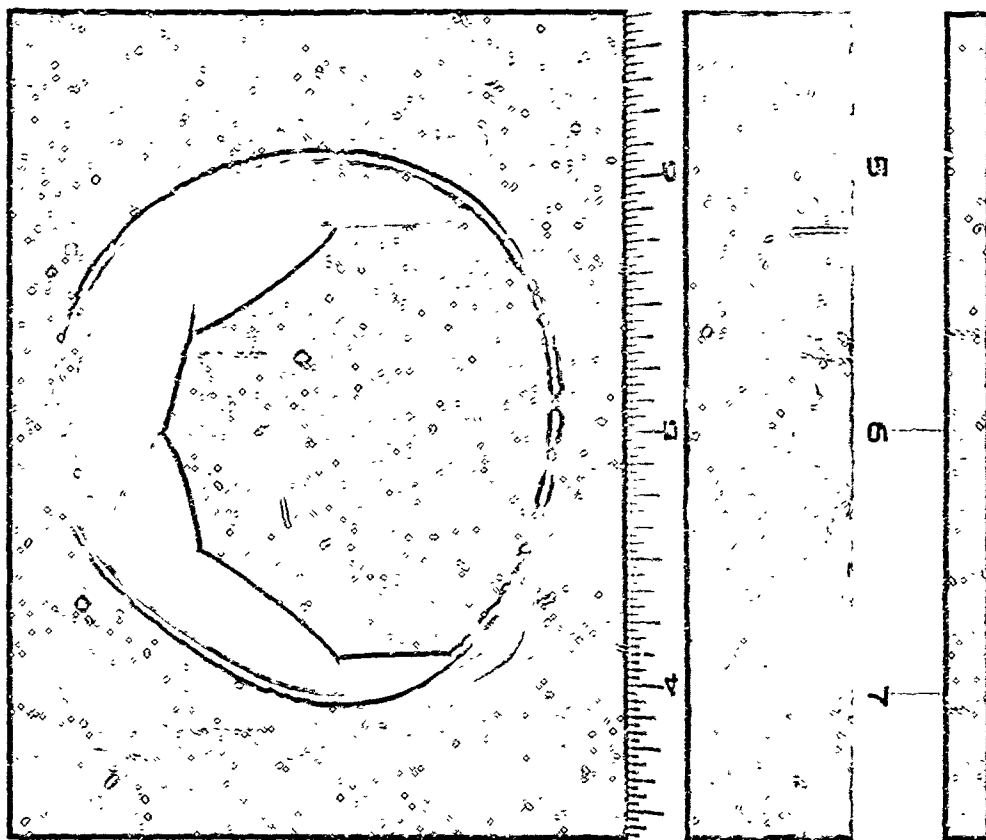


Fig. 14 Section View of a Shell Buckled in the Antisymmetric Mode, Specimen V-4

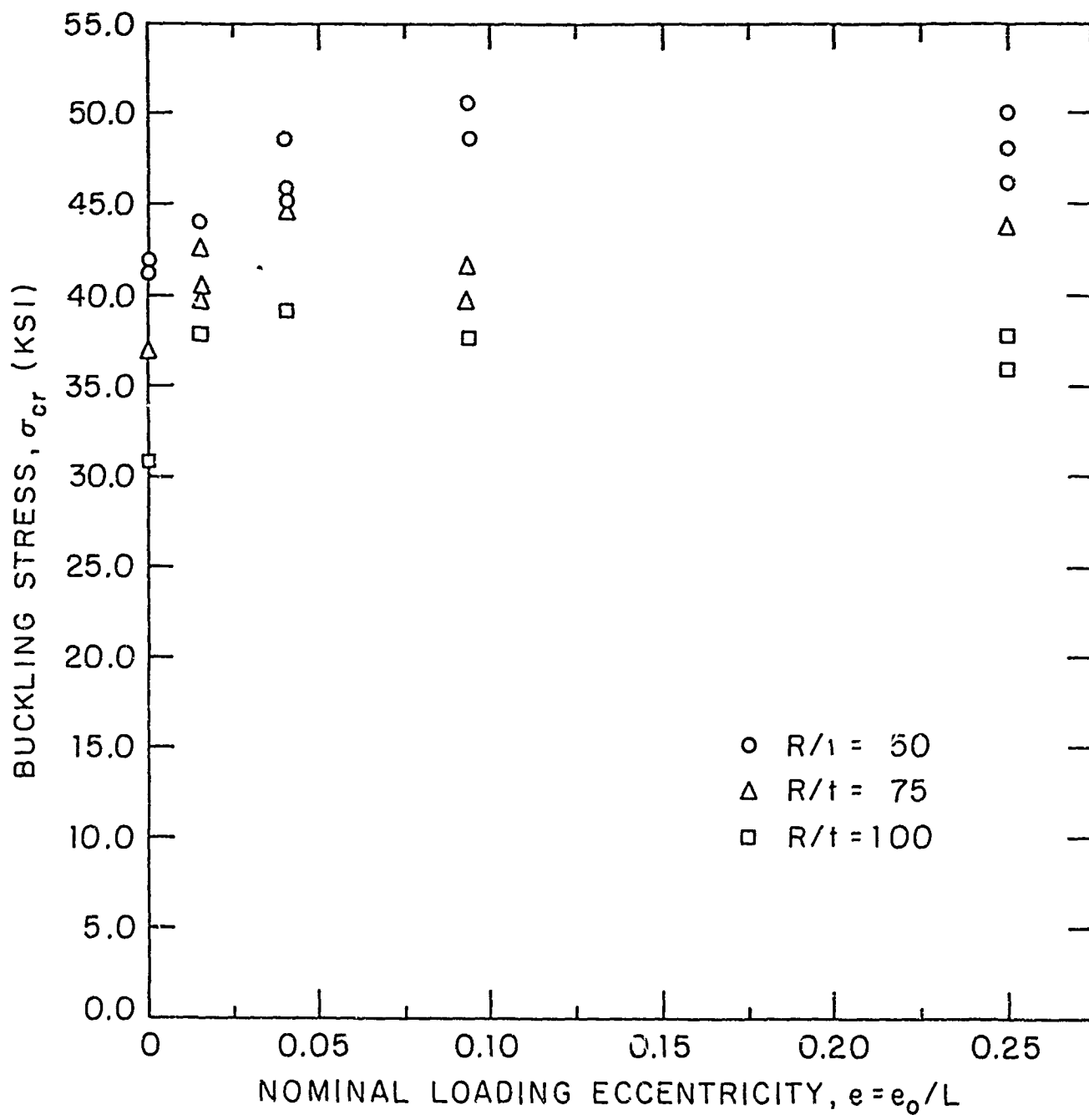


Fig. 15 Incipient-Buckling Stress as a Function of R/t and Loading Eccentricity

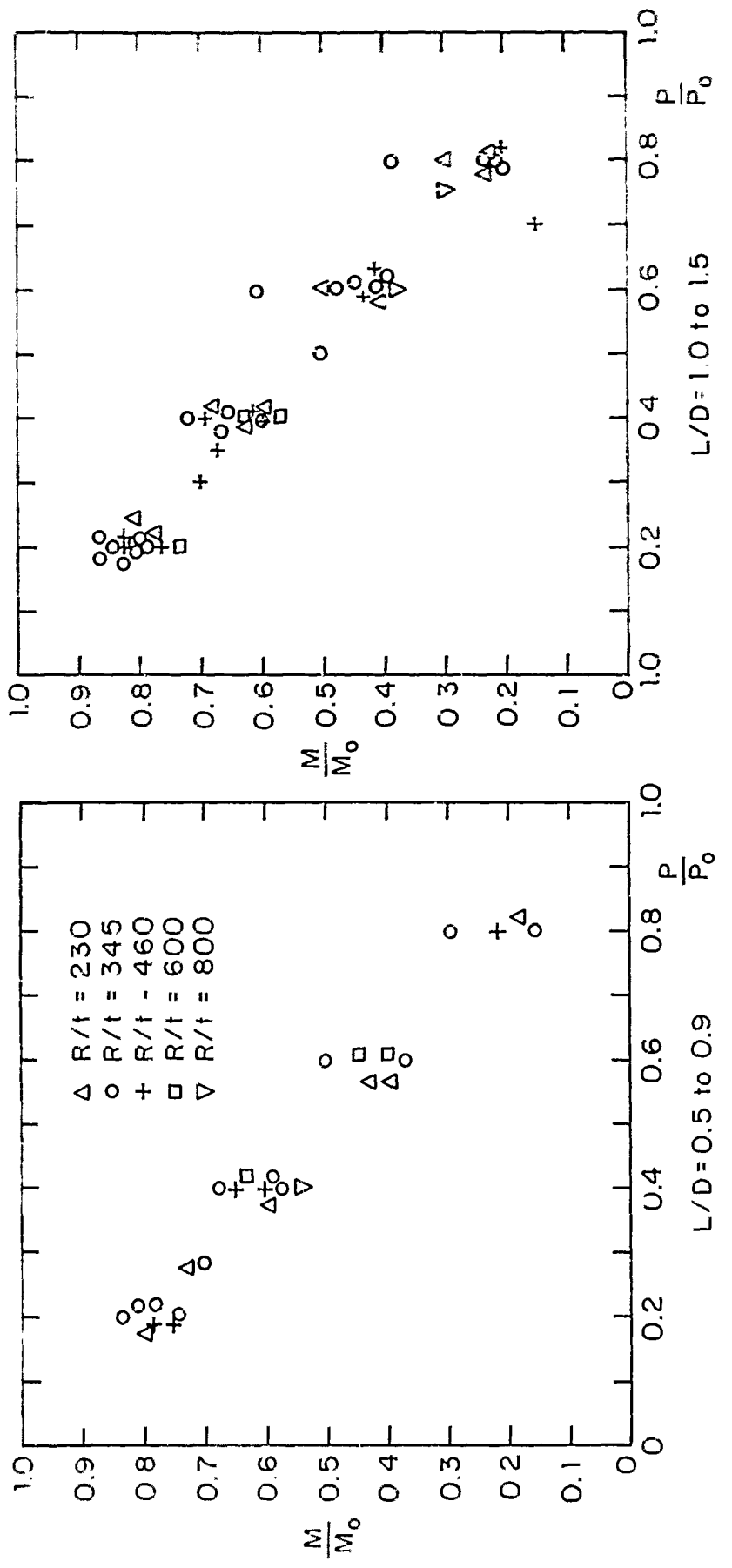


Fig. 16 Combined-Load Incipient-Buckling Data for Unstiffened Cylinders with R/t Values Ranging From 230 to 800 and L/D Values Ranging from 0.5 to 1.5 [Ref. 2]

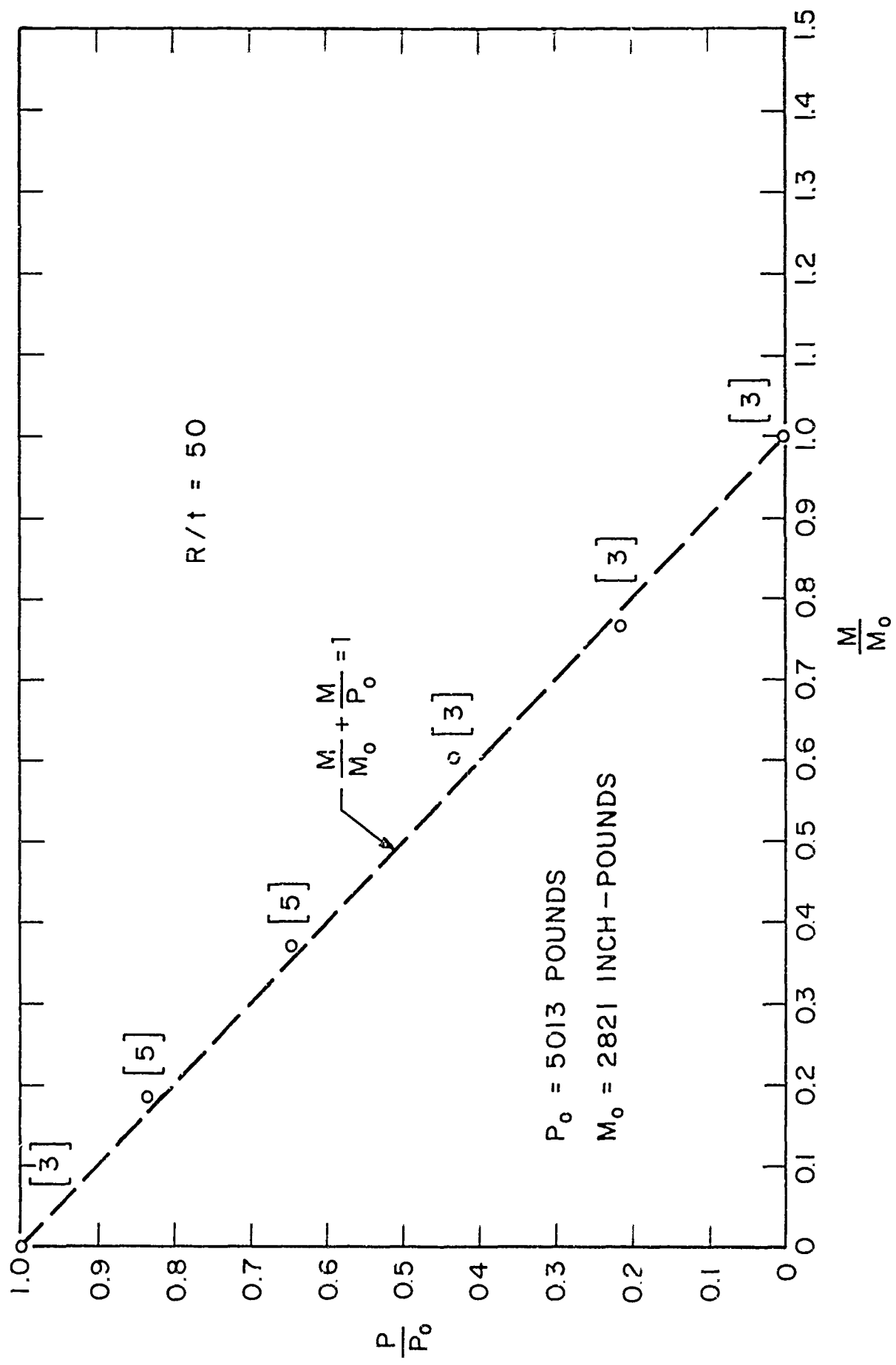


Fig. 17 Combined-Load Buckling-Threshold Data for $R/t = 50$

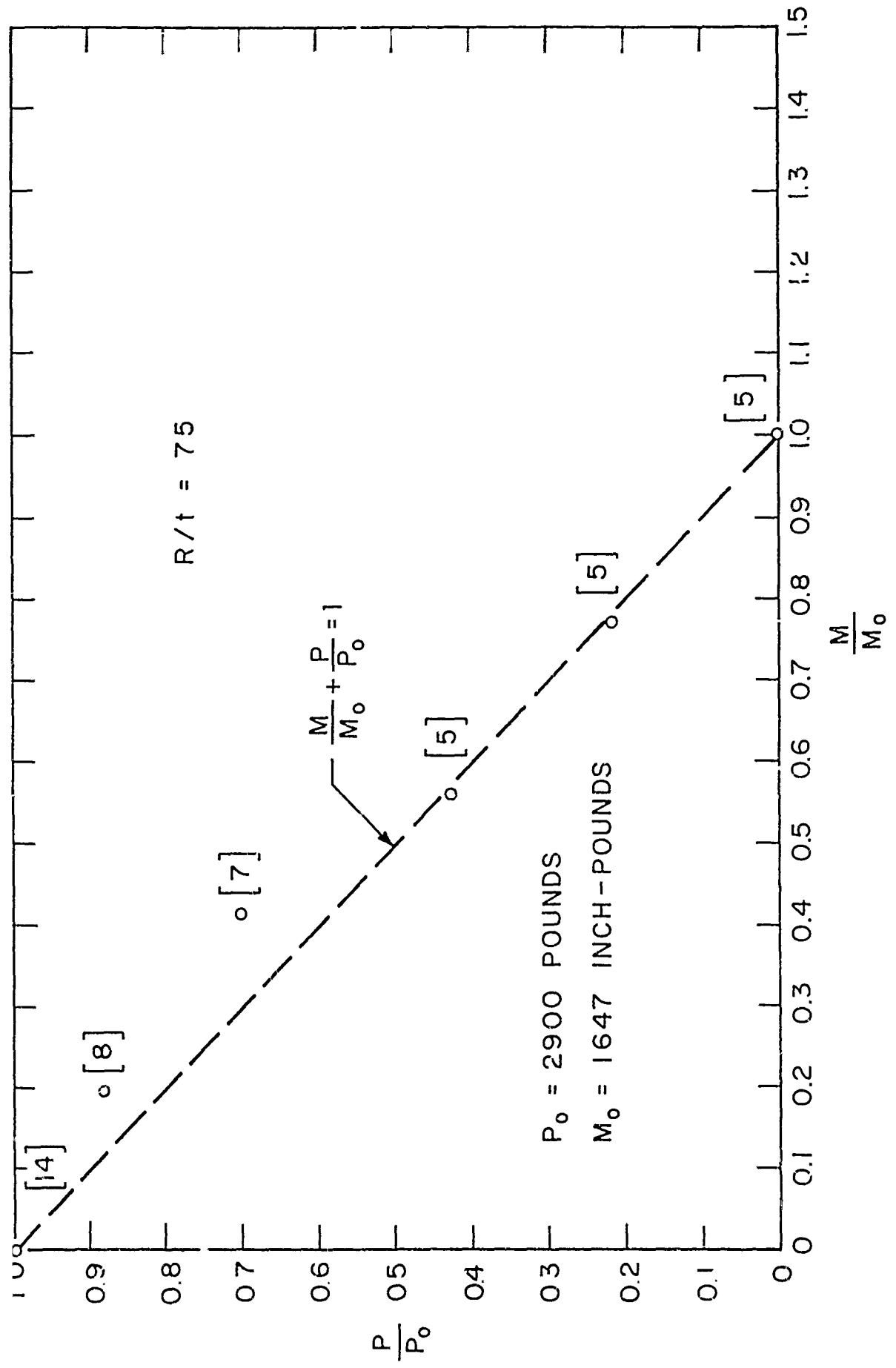


Fig. 18 Combined-Load Buckling-Threshold Data for $R/t = 75$

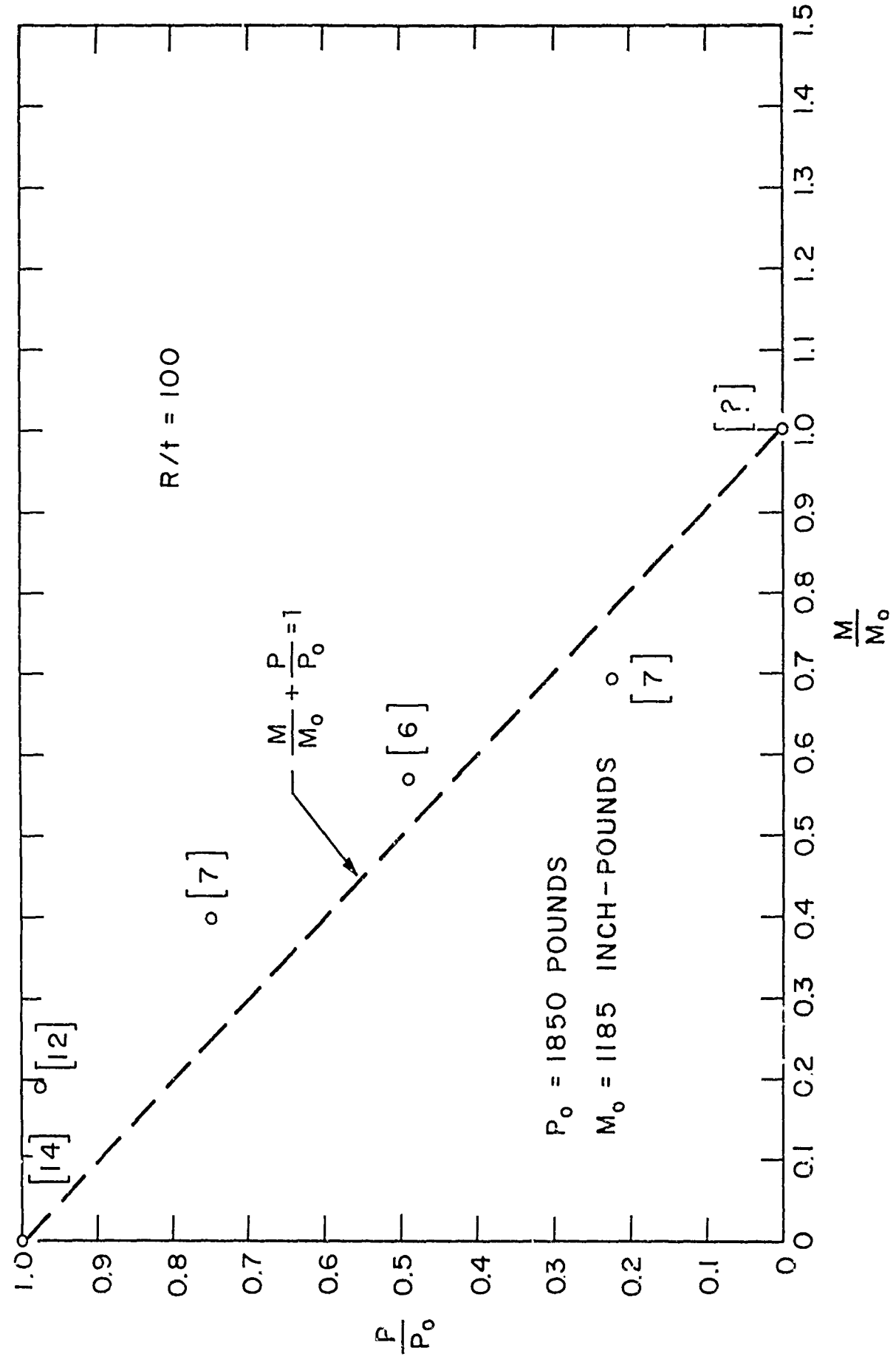
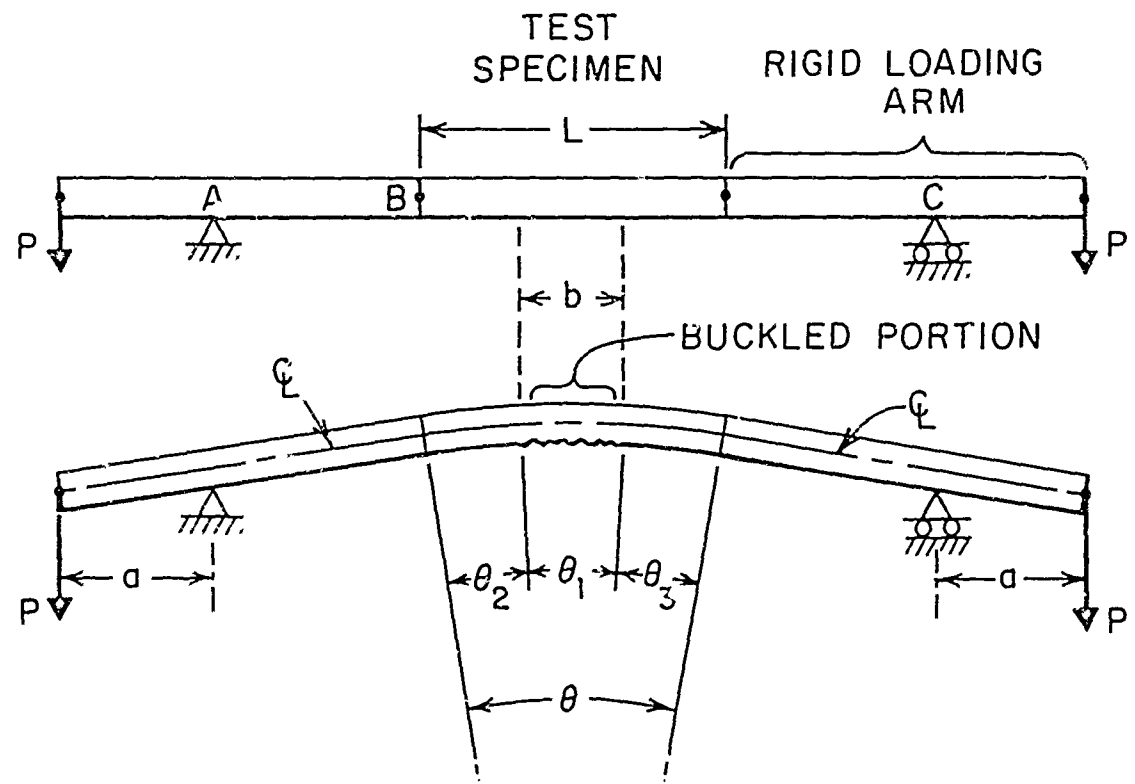
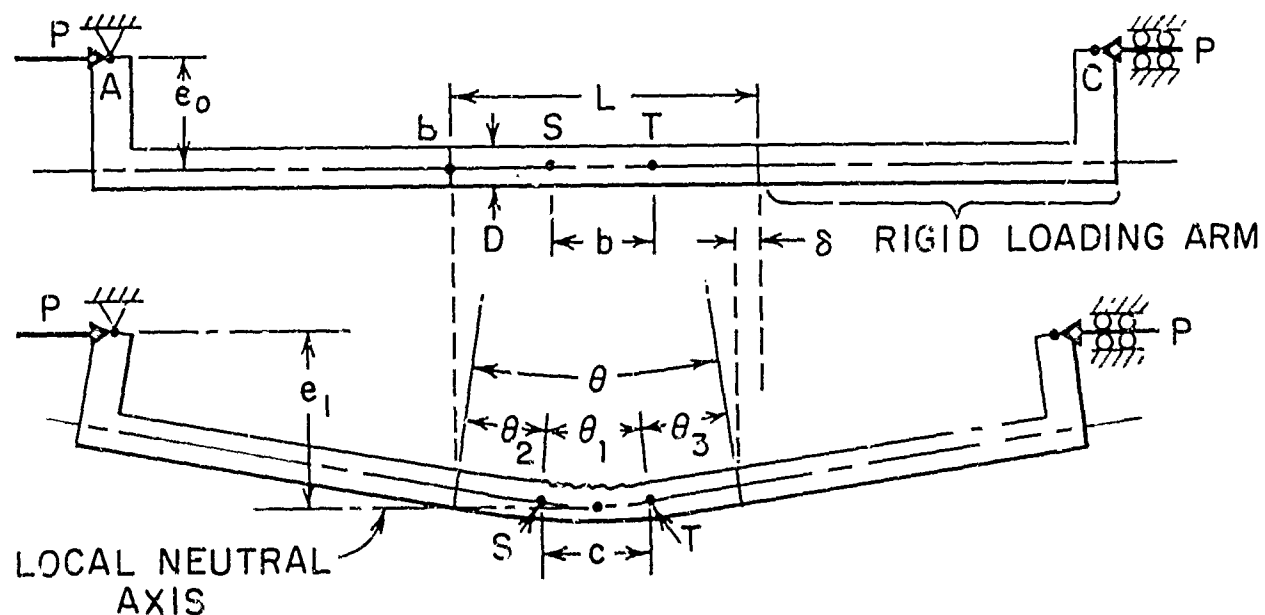


Fig 19 Combined-Load Buckling-Threshold Data for $R/t = 100$

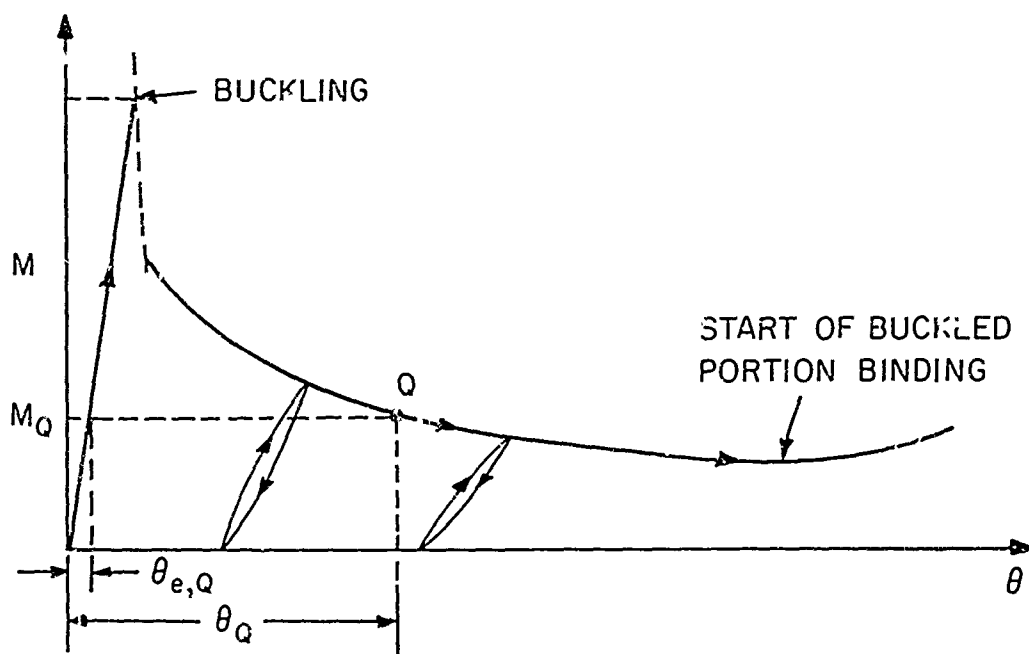


(a) Pure Bending

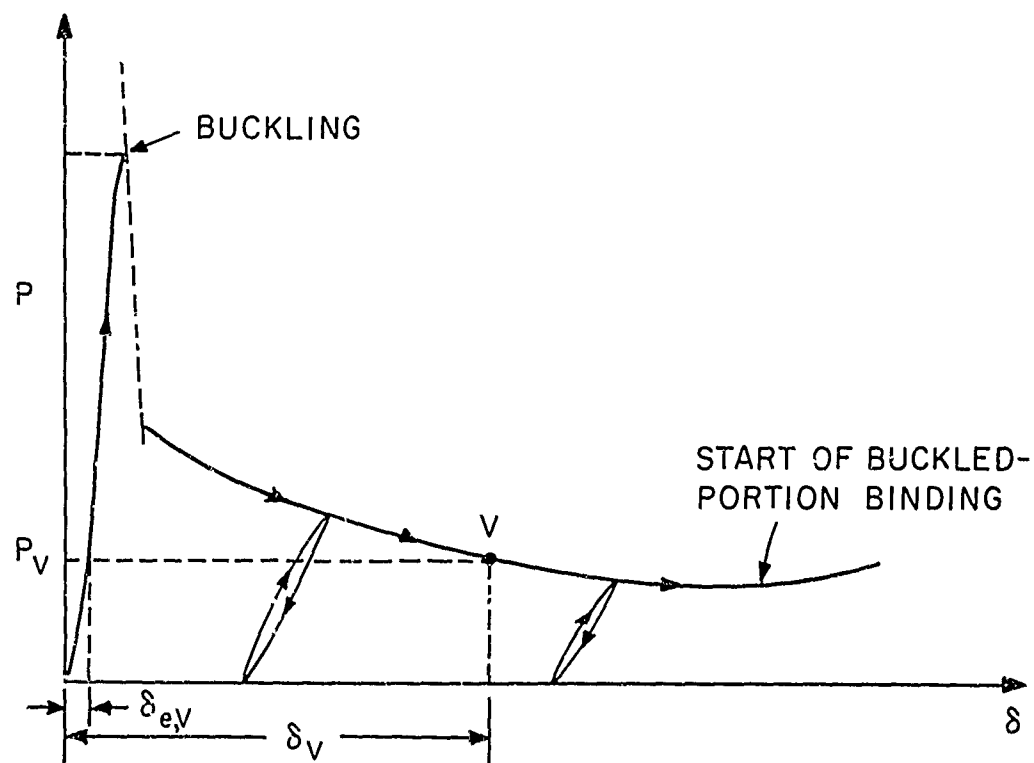


(b) Combined Axial Load and Bending

Fig. 20 Geometry and Nomenclature for a Buckled Specimen



(a) Moment - Deflection



(b) Axial Load, Axial Shortening

Fig. 21 Nomenclature and Typical Load-Deflection Characteristics of a Loaded Specimen in Both the Prebuckling and the Postbuckling Regime

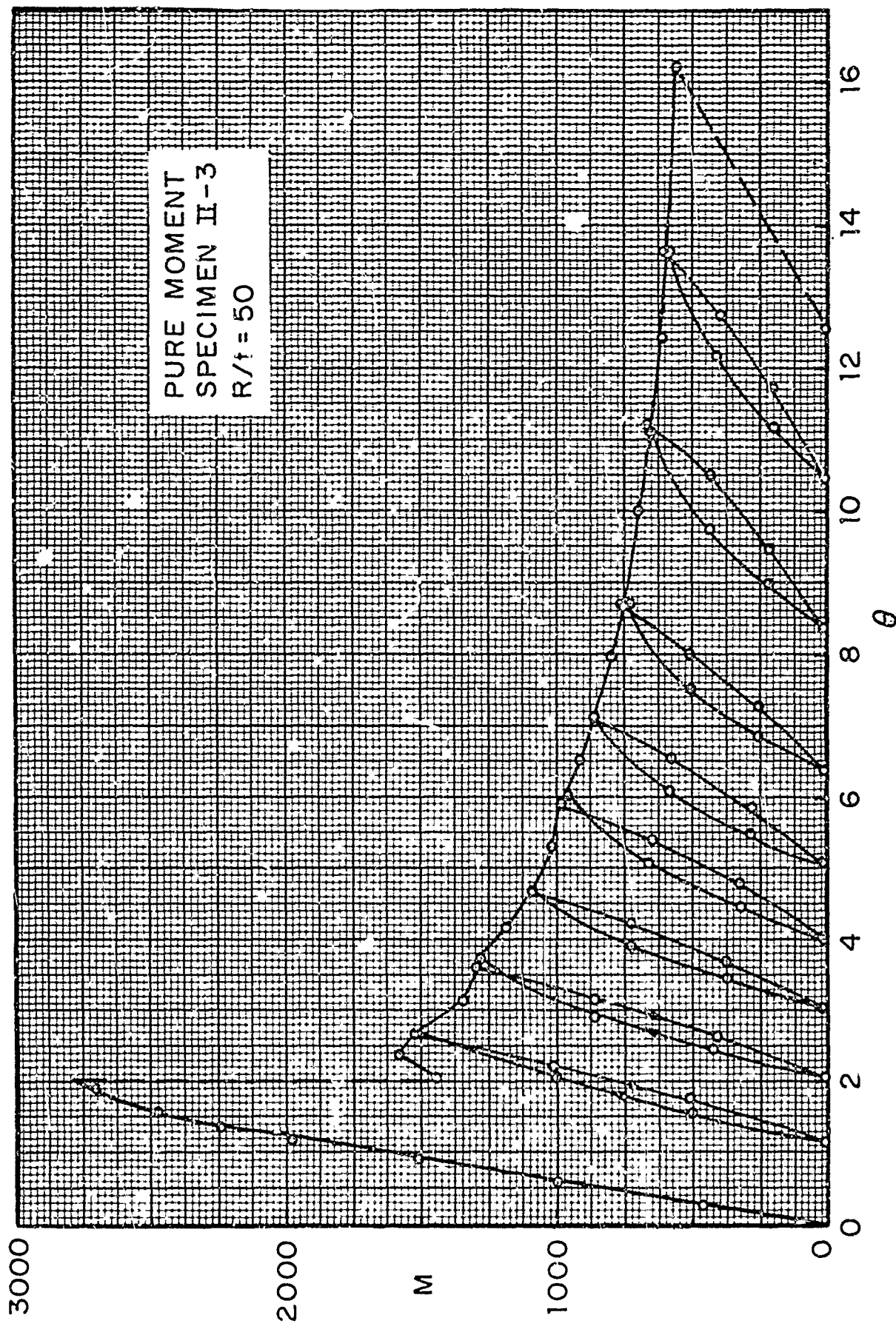


Fig. 22 Typical Prebuckling and Postbuckling Moment-Rotation Data for a Specimen Subjected to Pure Bending,
 $R/t = 50$

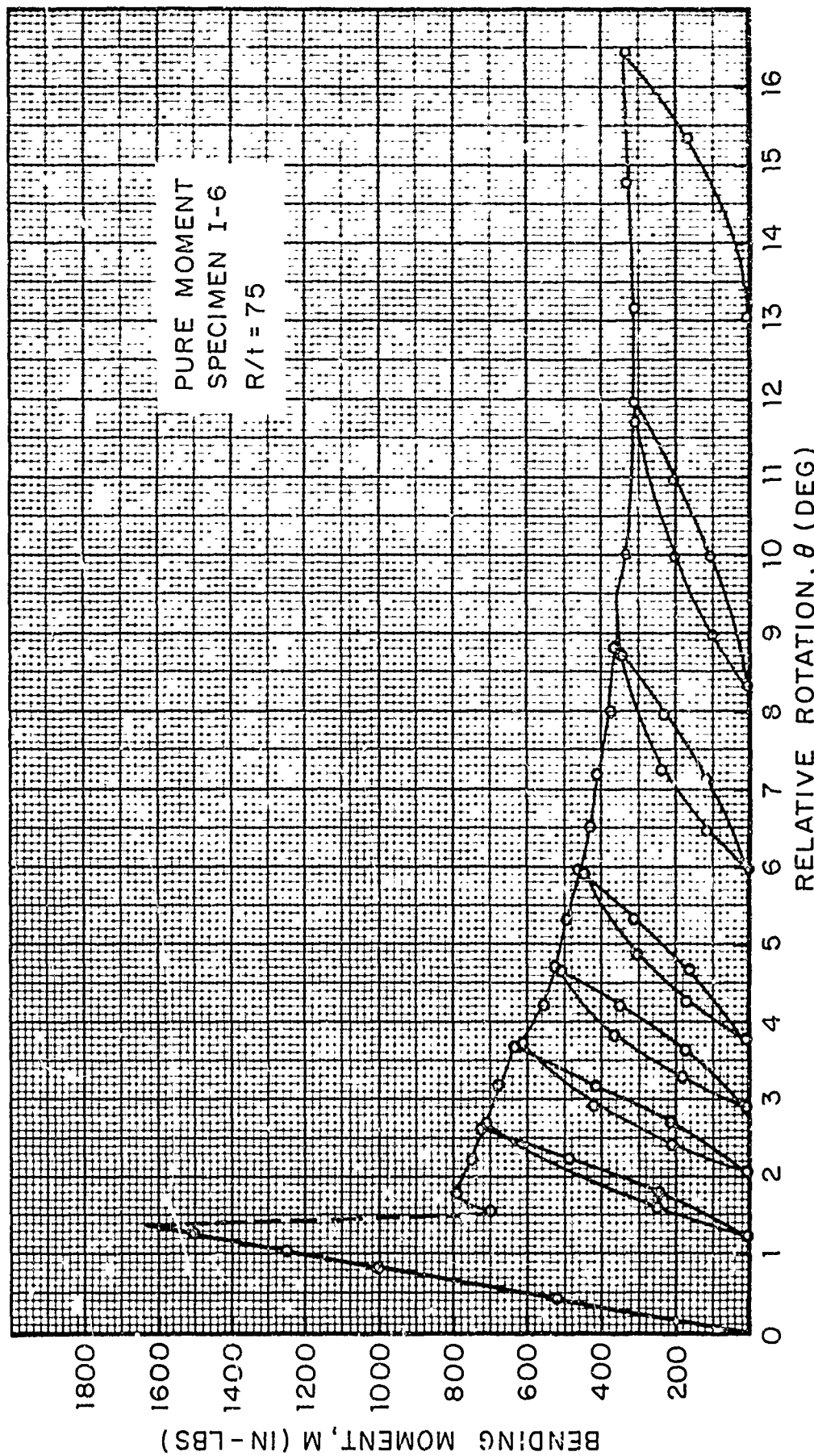


Fig. 23 Typical Prebuckling and Postbuckling Moment-Rotation Data for a Specimen Subjected to Pure Bending,
 $R/t = 75$

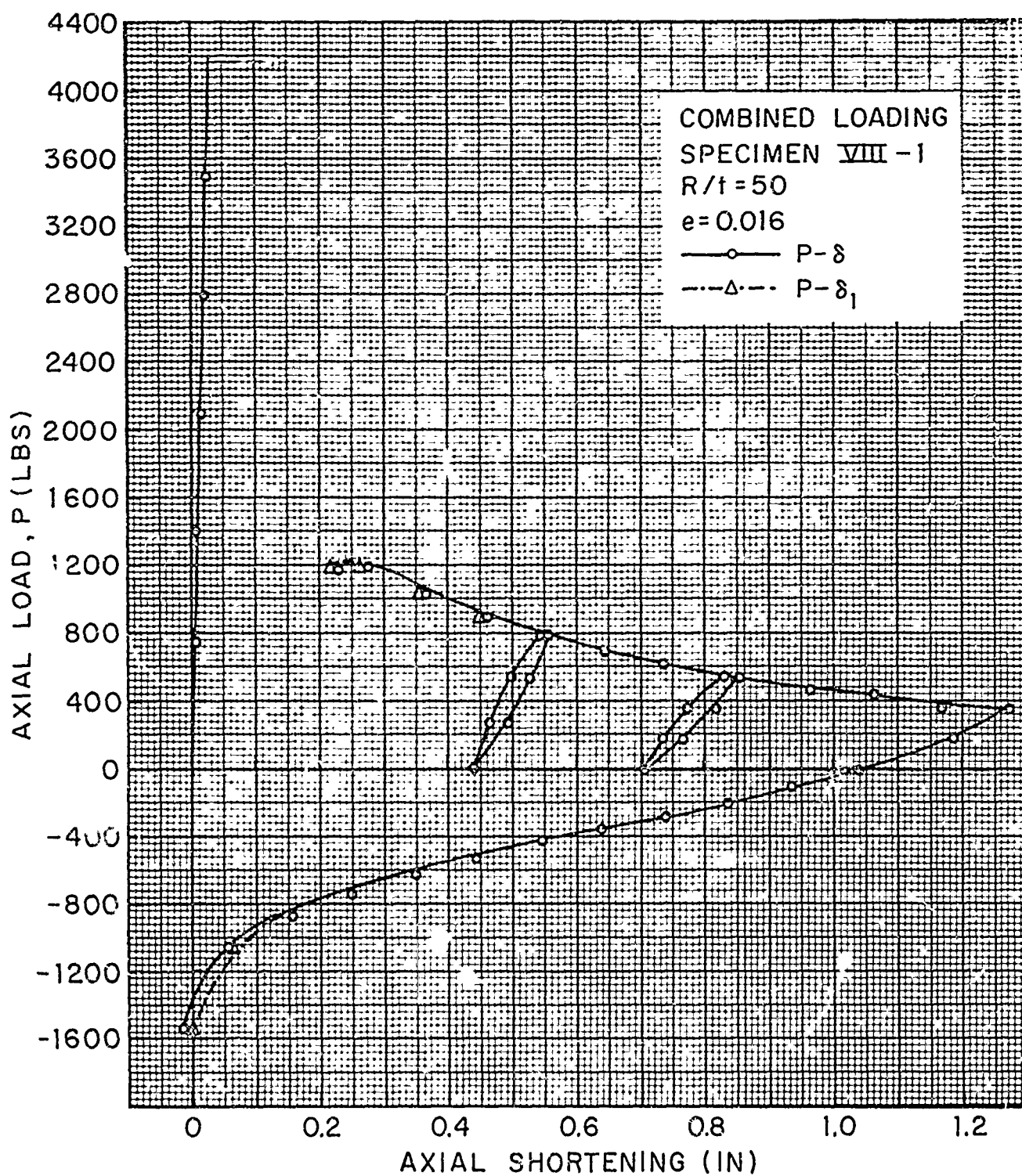


Fig. 24 Typical Prebuckling and Postbuckling Moment-Rotation and Load-Shortening Data, $R/t = 50$ and $e = 0.016$

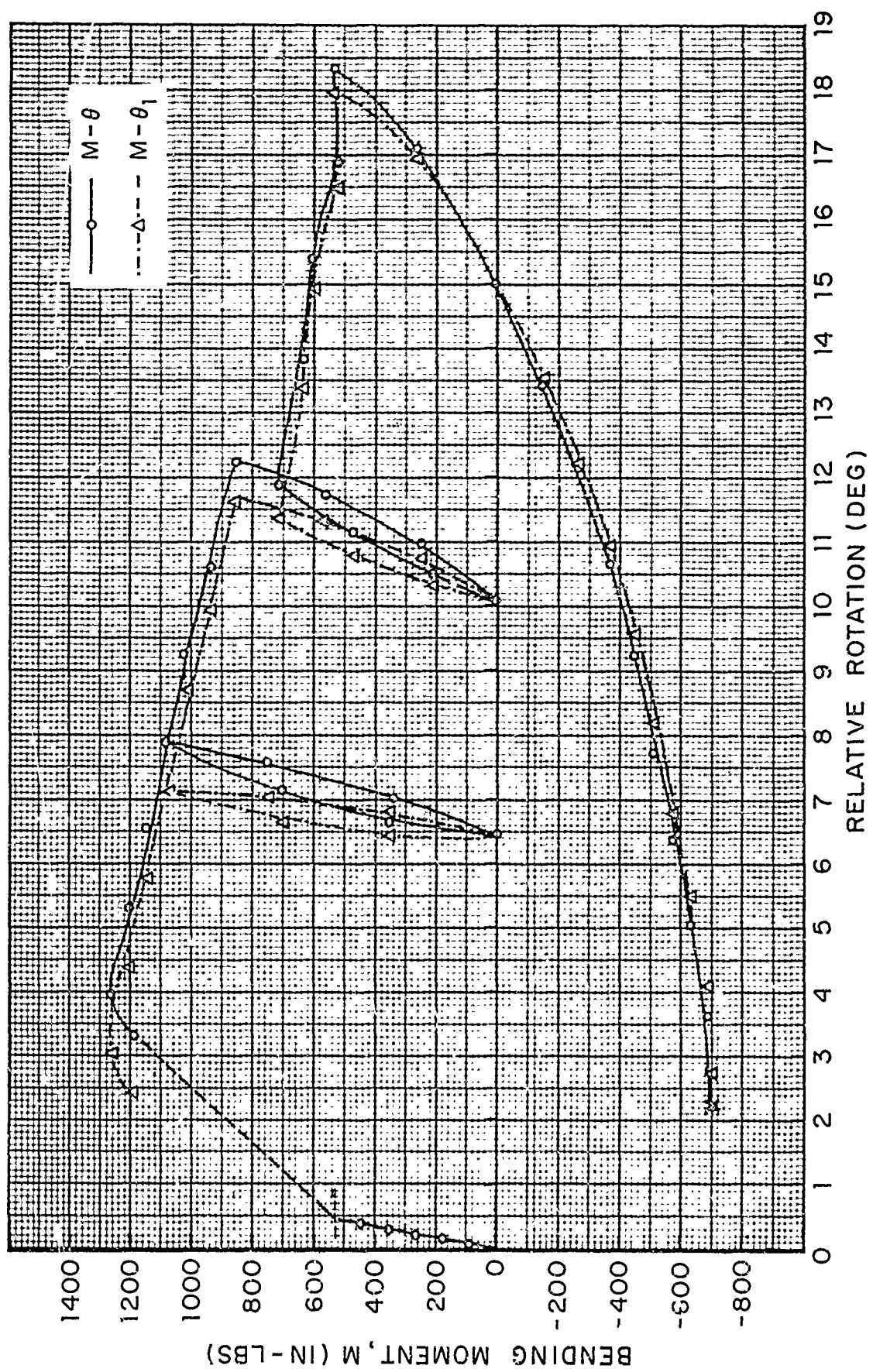


Fig. 24 Concluded

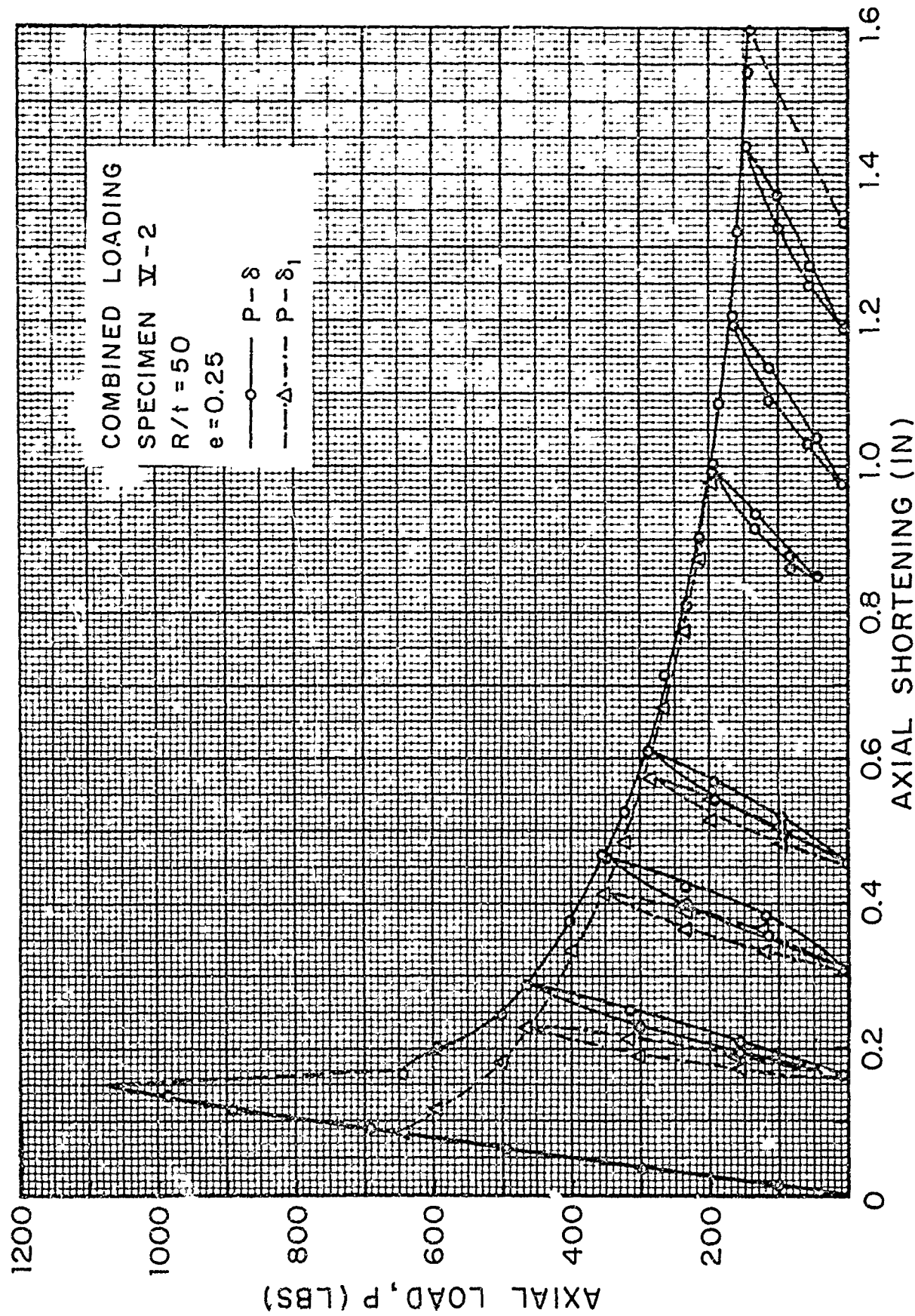


Fig. 25 Typical Prebuckling and Postbuckling Moment-Rotation and Load-Shortening Data, $R/t = 50$ and $e = 0.25$

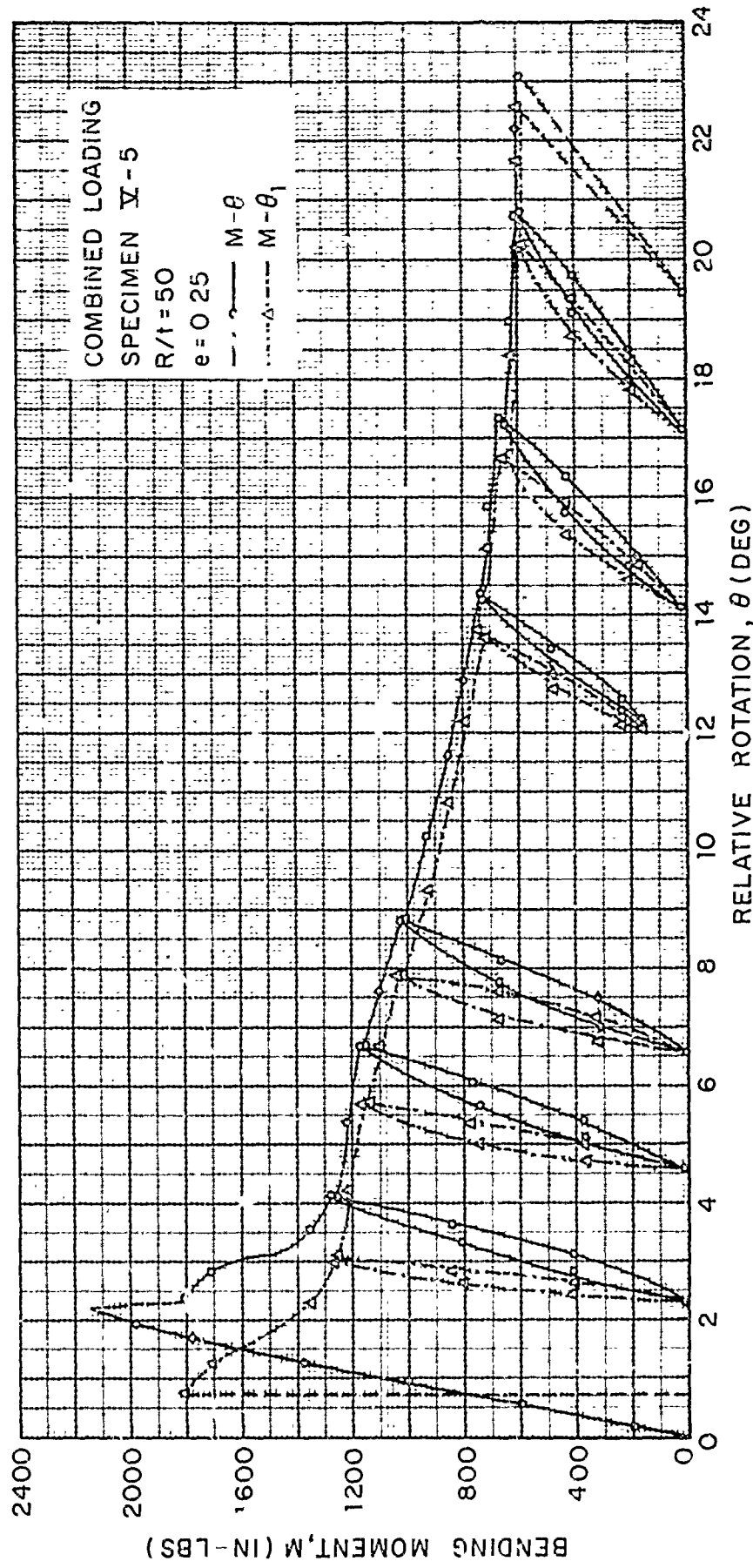


Fig. 25 Concluded

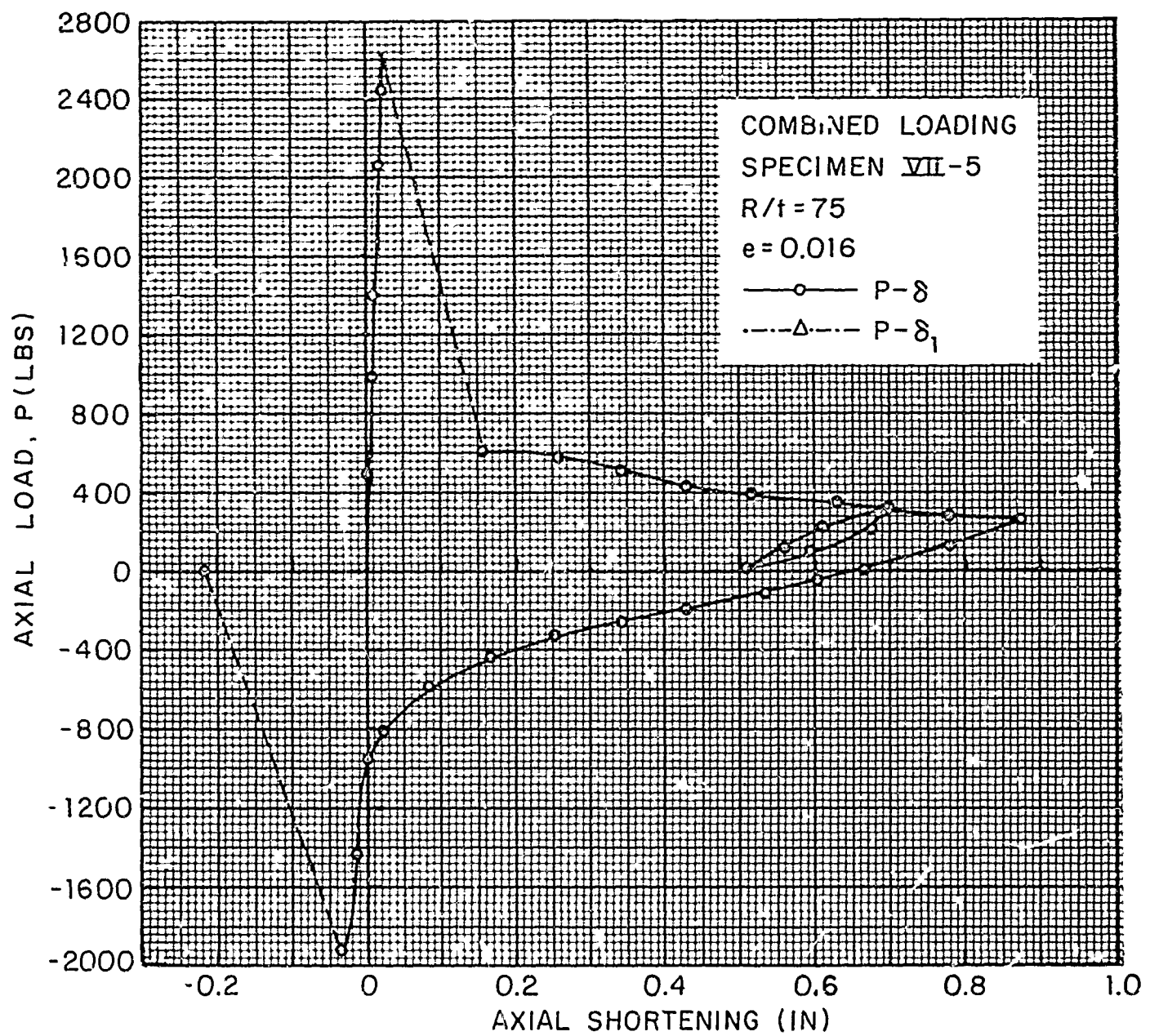


Fig. 26 Typical Prebuckling and Postbuckling Moment-Rotation and Load-Shortening Data, $R/t = 75$, $e = 0.016$

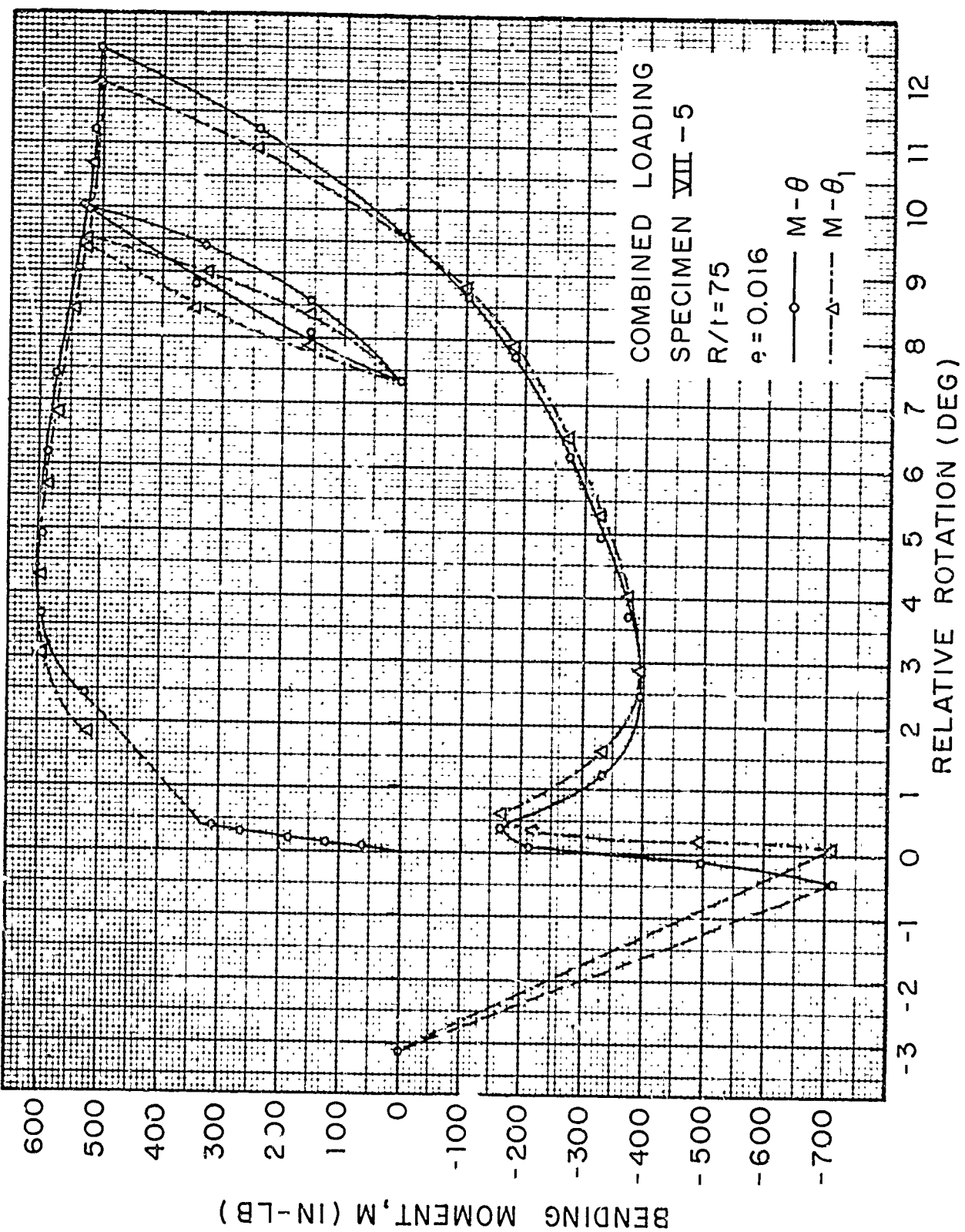


Fig. 26 Concluded

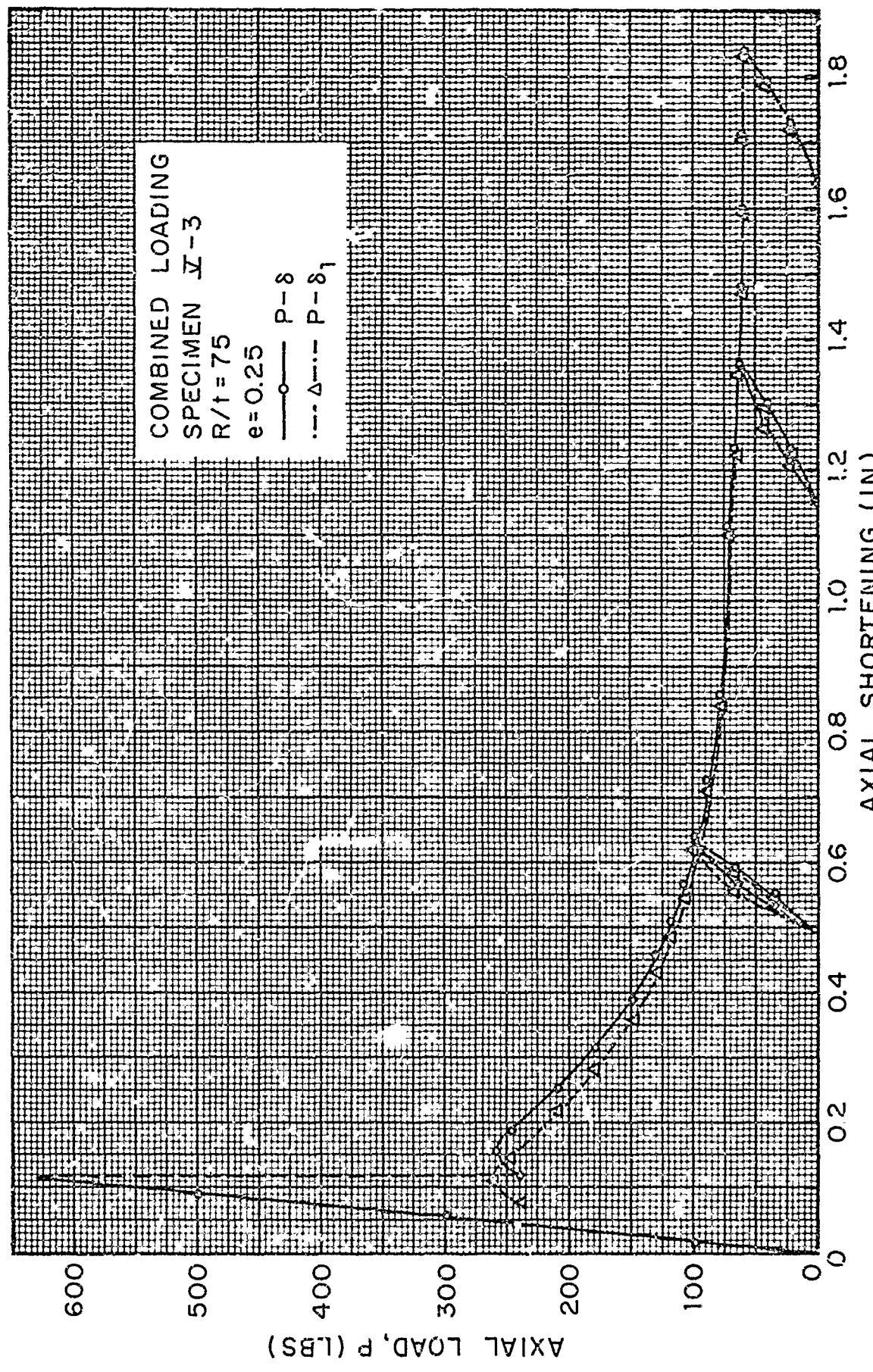


Fig. 27 Typical Prebuckling and Postbuckling Moment-Rotation and Load-Shortening Data, $R/t = 75$, $e = 0.25$

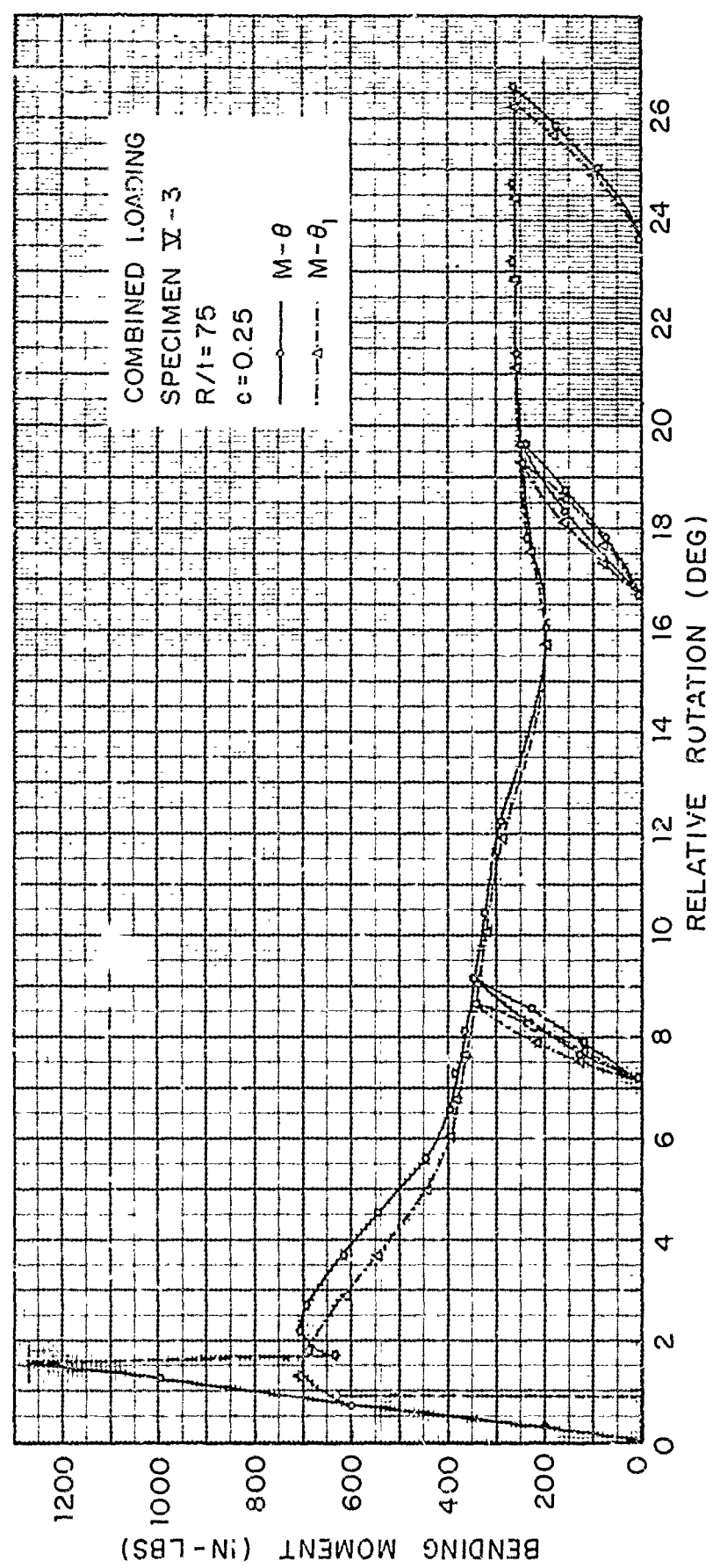


Fig. 27 Concluded

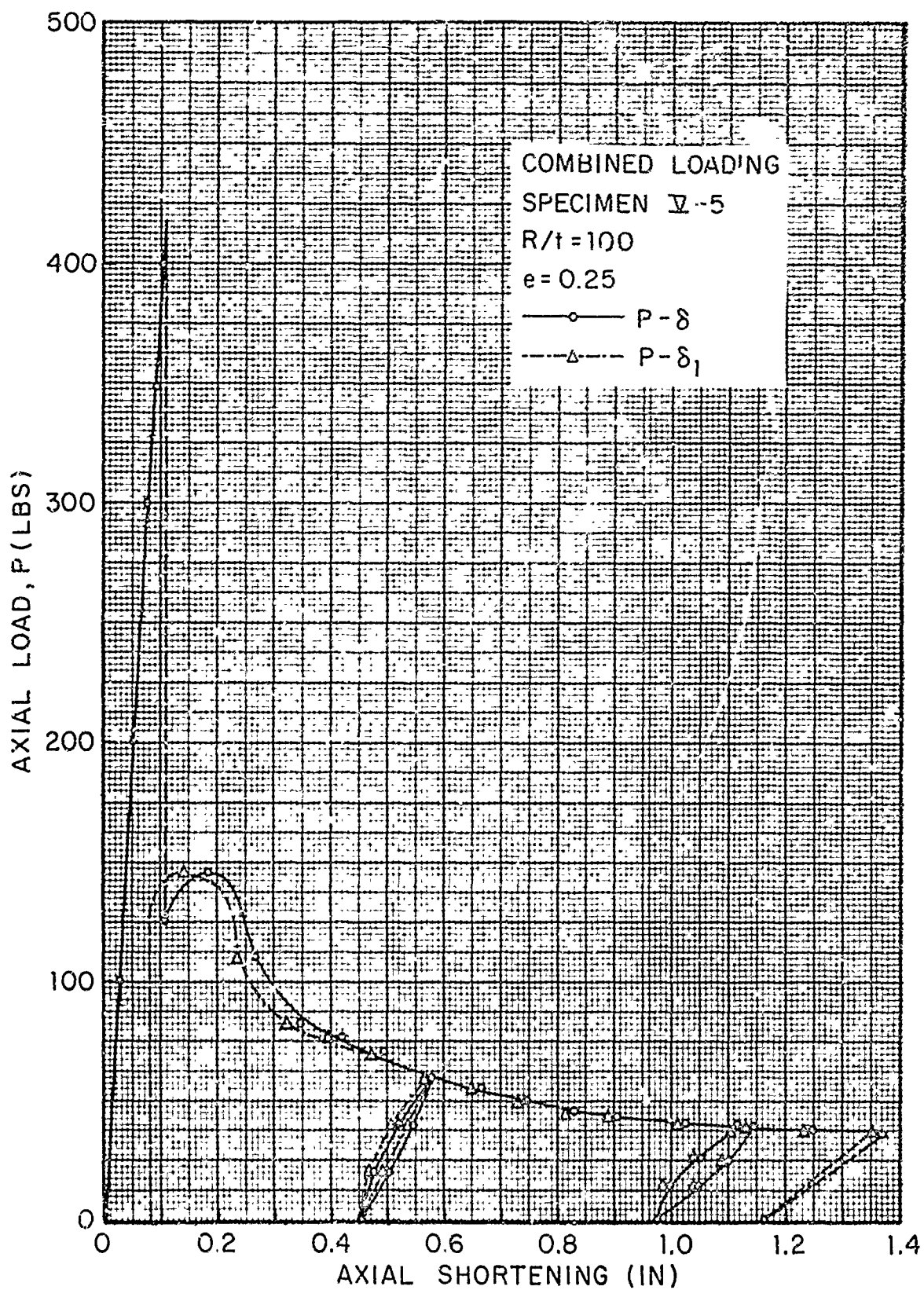


Fig. 28 Typical Prebuckling and Postbuckling Moment-Rotation and Load-Shortening Data, $R/t = 100$, $e = 0.25$

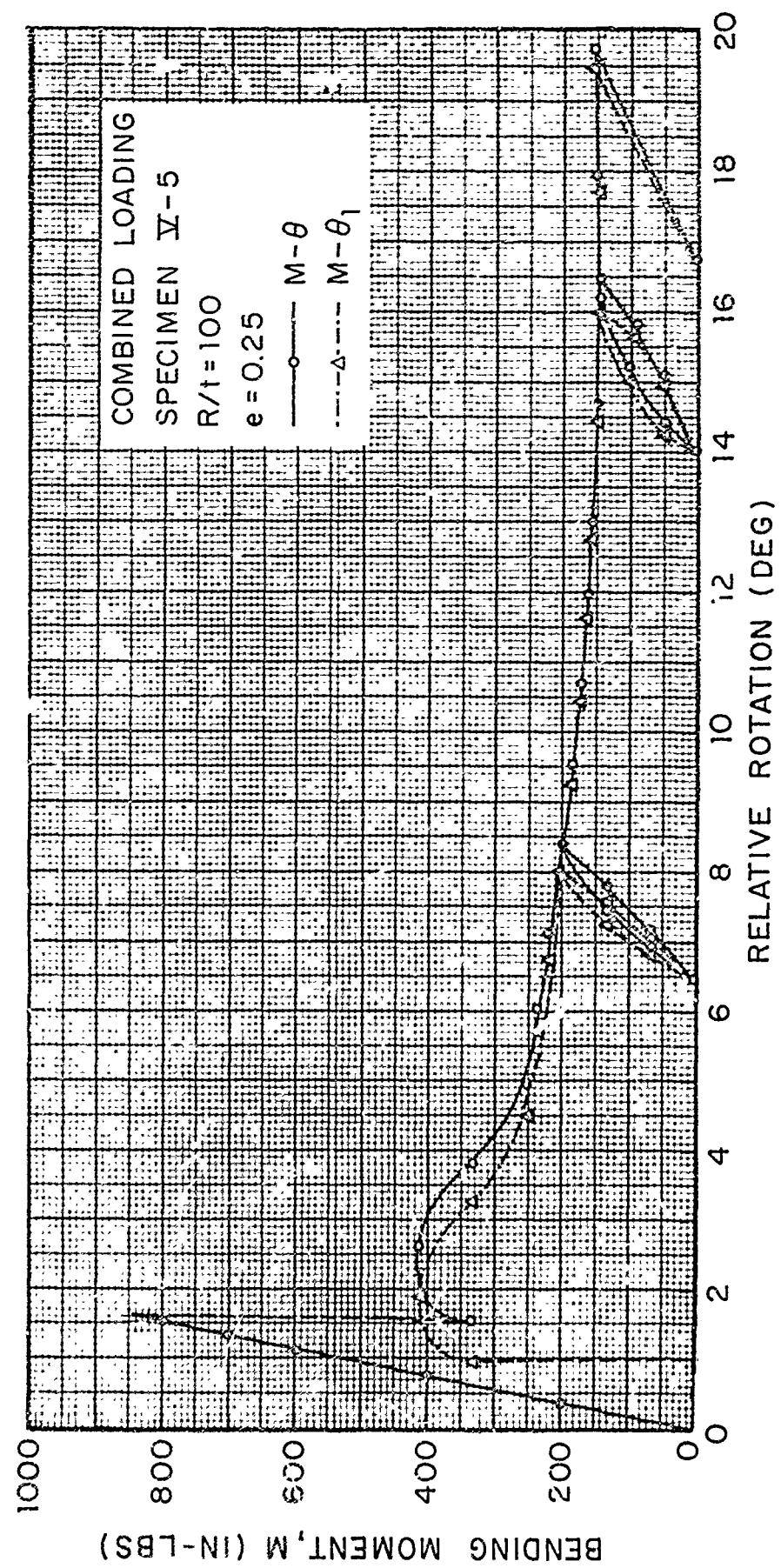


Fig. 28 Concluded